

Interactions, star formation and extended nebulae in SDSS type 2 quasars at $0.3 \leq z \leq 0.6$ [★]

M. Villar-Martín,^{1†} C. Tadhunter,² A. Humphrey,³ R. Fraga Encina,⁴
R. González Delgado,¹ M. Pérez Torres¹ and A. Martínez-Sansigre⁵

¹*Instituto de Astrofísica de Andalucía (CSIC), Glorieta de la Astronomía s/n, 18008 Granada, Spain*

²*Department of Physics and Astronomy, University of Sheffield, Sheffield S3 7RH*

³*Instituto Nacional de Astrofísica, Óptica y Electrónica (INAOE), Aptdo. Postal 51 y 216, 72000 Puebla, Mexico*

⁴*Instituto de Física de Cantabria (CSIC-UC), Avda. de los Castros, s/n, E-39005 Santander, Spain*

⁵*Institute of Cosmology and Gravitation, University of Portsmouth, Dennis Sciama Building, Burnaby Road, Portsmouth PO1 3FX*

Accepted 2011 May 9. Received 2011 May 6; in original form 2011 January 28

ABSTRACT

We present long-slit spectroscopy and imaging data obtained with the Focal Reducer and Low Dispersion Spectrograph (FORS2) on the Very Large Telescope of 13 optically selected type 2 quasars at $z \sim 0.3$ – 0.6 from the original sample of Zakamska et al. (2003). The sample is likely to be affected by different selection biases. We investigate the evidence for (i) mergers/interactions (ii) star formation activity in the neighbourhood of the quasars and (iii) extended emission-line regions (EELRs) and their nature. Evidence for mergers/interactions is found in 5/13 objects. This is a lower limit for our sample, given the shallowness of most of our continuum images. Although active galactic nucleus (AGN) photoionization cannot be totally discarded, line ratios consistent with stellar photoionization are found in general in companion galaxies/knots/nuclei near these same objects. On the contrary, the gas in the neighbourhood of the quasar nucleus shows line ratios inconsistent with H II galaxies and typical of AGN photoionized nebulae. A natural scenario to explain the observations is that star formation is ongoing in companion galaxies/knots/nuclei, possibly triggered by the interactions. These systems are, therefore, composite in their emission-line properties showing a combination of AGN and star formation features.

EELRs have been found in 7/13 objects, although this fraction might be higher if a complete spatial coverage around the quasars was performed. The sizes vary between a few and up to 64 kpc. In general, the EELR apparently consists of an extended nebula associated with the quasar. In at least one case, the EELR is associated with ionized tidal features.

Key words: galaxies: active – quasars: emission lines – quasars: general.

1 INTRODUCTION

According to the standard unification model of active galactic nuclei (AGNs) certain classes of type 1 and type 2 AGNs are the same entities, but have different orientations relative to the observer's line of sight (e.g. Seyfert 1s and 2s; Antonucci 1993). An obscuring structure blocks the view to the inner nuclear region for some orientations. If this model is valid for the most luminous AGNs (quasars), there must exist a high-luminosity family of type 2 quasars. The existence of this object class was predicted a long

time ago, but it has been only in the last few years that type 2 quasars have been discovered in large quantities (e.g. Zakamska et al. 2003; Martínez-Sansigre et al. 2005). In particular, Zakamska et al. identified in 2003 ~ 300 objects in the redshift range $0.3 \leq z \leq 0.8$ in the Sloan Digital Sky Survey (SDSS; York et al.) with the high-ionization narrow emission-line spectra characteristic of type 2 AGNs and narrow line luminosities typical of type 1 quasars. Their far-infrared luminosities place them among the most luminous quasars at similar z . They show a wide range of X-ray luminosities and obscuring column densities (Zakamska et al. 2004; Ptak et al. 2006). The host galaxies are often ellipticals with irregular morphologies (Zakamska et al. 2006), and the nuclear optical emission is highly polarized in some cases (Zakamska et al. 2005). The detection rate at 1.4 GHz in the Faint Images of the Radio Sky at Twenty centimetres (FIRST) survey is ~ 49 per cent (Zakamska et al. 2004). Lal & Ho (2010) found a detection rate ~ 59 per cent

[★]Based on observations carried out at the European Southern Observatory (Paranal, Chile) with FORS2 on VLT-UT1 (programmes 081.B-0129, 083.B-0381 and 087.B-0034).

[†]E-mail: montse@iaa.es

at 8.4 GHz using nearly one order of magnitude deeper Very Large Array images. 15 ± 5 per cent qualify as radio loud.

We are undertaking an imaging and spectroscopic observational programme using FORS2 on the Very Large Telescope (VLT) to perform detailed optical imaging and spectroscopic studies of SDSS type 2 quasars and address several critical aspects related to the nuclear activity and the evolution of massive elliptical galaxies.

(1) *The triggering mechanism of the nuclear activity.* Both models and observations of powerful type 1 quasars and radio galaxies support the idea that major mergers and interactions are an efficient mechanism to trigger the nuclear activity in the most powerful AGN (e.g. Ramos Almeida et al. 2011), although some authors challenge this interpretation (e.g. Cisternas et al. 2011). We are addressing this issue by searching for signatures of mergers/interactions in the environment of SDSS type 2 quasars.

(2) *The existence of associated extended emission line regions (EELRs).* Previous works show that luminous EELRs ($L[\text{O III}]_{\text{EELR}} \geq 5 \times 10^{41} \text{ erg s}^{-1}$) around type 1 quasars at $z \leq 0.5$ exist preferentially associated with steep-spectrum radio-loud quasars with luminous nuclear emission lines ($L[\text{O III}]_{\text{nuc}} \geq 6.5 \times 10^{42} \text{ erg s}^{-1}$) and low broad-line region (BLR) metallicities ($Z \leq 0.6 Z_{\odot}$, although it must be kept in mind that metallicity estimations are highly uncertain). The EELRs have low metallicities and they also seem specially prevalent in quasars showing signs of strong galaxy interactions (e.g. Fu & Stockton 2009, 2007). The more frequent occurrence of luminous EELRs in radio-loud objects suggests that their origin might be connected with the radioactivity (ejection?) or, alternatively, that the radioactivity is only triggered in rich gaseous environments. Since very little is known about the existence of EELRs in type 2 quasars, we are addressing this issue in our observational programme by searching for such nebulae and characterizing their general properties. The SDSS type 2 quasar sample is good for testing the potential importance of nuclear emission-line luminosity on the existence of EELR, since they are mostly radio quiet and have large nuclear line luminosities. Greene et al. (2011) have recently found that ionized gas at spatial scales $\gtrsim 10 \text{ kpc}$ is rare in SDSS type 2 quasars at surface brightness (SB) levels $\sim 10^{-16} \text{ erg s}^{-1} \text{ cm}^{-2} \text{ arcsec}^{-2}$. Our data reach SB levels $\gtrsim 20$ times deeper.

(3) *Quasar feedback processes.* Quasar-induced outflows are recognized as an important feedback mechanism on the formation of massive elliptical galaxies. Studies of powerful radio-loud AGNs suggest that radio jet induced outflows can have enormous energies sufficient to eject a large fraction of the gaseous galaxy content (Humphrey et al. 2006; Nesvadba et al. 2006). However, the majority of quasars are radio quiet (e.g. Jiang et al. 2007). How AGN feedback works in these objects is still an open question.

Type 2 quasars are unique laboratories to investigate these issues. The occultation of the active nucleus by the obscuring torus allows a detailed study of many properties of the surrounding medium, which is difficult in type 1 quasars due to the dominant contribution of the quasar point spread function. On the other hand, the radioactivity in radio-loud quasars and radio galaxies often imprints important distortions on the observed optical properties via jet–gas interaction. This complicates the characterization of the intrinsic properties of the host galaxy and environment. Type 2 quasars can help to identify and understand those phenomena that are not related to the radio activity.

In Villar-Martín et al. (2010), we published the first results of our VLT programme for SDSS J0123+00 at $z = 0.4$. We discovered that this quasar, which is a member of an interacting system, is

physically connected to a companion galaxy by a $\geq 100 \text{ kpc}$ filament which is possibly forming stars actively. The origin of the EELR in this particular case is a galaxy interaction, and our results showed that luminous EELR can also be associated with low radio luminosity quasars, in contrast to expectations based on type 1 quasar studies.

We present in this paper the results based on VLT spectroscopic and imaging data of 13 more SDSS type 2 quasars regarding issues (1) and (2) mentioned above. A detailed study of feedback mechanisms in this sample will be presented in Villar-Martín et al. (in preparation).

We assume $\Omega_{\Lambda} = 0.7$, $\Omega_{\text{M}} = 0.3$, $H_0 = 71 \text{ km s}^{-1} \text{ Mpc}^{-1}$.

2 SAMPLE SELECTION, OBSERVATIONS AND DATA REDUCTION

The data were obtained with the Focal Reducer and Low Dispersion Spectrograph (FORS2) for the VLT installed on UT1 (Appenzeller et al. 1998). The observations were performed in two different runs: 2008 September 8 and 9 (four objects) and 2009 April 17 and 18 (nine objects). The broad-band image of SDSS J1307–02 presented in this paper was obtained on 2011 April 28.

Three criteria were common to all 13 objects studied in this paper.

(1) They are type 2 quasars extracted from Zakamska et al. (2003) SDSS sample. They are radio quiet in general ($P_{5 \text{ GHz}} < 10^{31} \text{ erg s}^{-1} \text{ Hz}^{-1} \text{ sr}^{-1}$ according to the criteria by Miller, Peacock & Mead (1990); we assume $P_{\nu} \propto \nu^{-\alpha}$, with $\alpha = 0.7$). The only exception is SDSS 1228+00, which has $P_{5 \text{ GHz}} = 2.4 \times 10^{31} \text{ erg s}^{-1} \text{ Hz}^{-1} \text{ sr}^{-1}$, in the transition range between radio-quiet and radio-loud objects ($P_{5 \text{ GHz}} > 10^{32} \text{ erg s}^{-1} \text{ Hz}^{-1} \text{ sr}^{-1}$).

(2) The SDSS optical spectra show emission lines with large equivalent widths. In this way, we avoid in most cases uncertainties due to underlying stellar absorption and ensure a high signal-to-noise ratio for the kinematic analysis. Objects with low line luminosities were *not* excluded. Because of their selection criteria, type 2 quasars in Zakamska et al. (2003) original sample have $L[\text{O III}]$ luminosities in the range $\sim [10^8 - 10^{10}] L_{\odot}$. The $L[\text{O III}]$ range in our sample is $[1.2 \times 10^8 - 4.1 \times 10^9] L_{\odot}$ as measured from the SDSS spectra.

(3) All objects have redshift $z \sim 0.3 - 0.6$ such that there was an adequate narrow- or intermediate-band FORS2 filter containing one of the strongest emission lines in the optical spectrum ($[\text{O II}]\lambda 3727$ or $[\text{O III}]\lambda 5007$).

Additional criteria were applied to 10/13 objects in the sample: they had prior evidence for mergers/interactions (one object) and/or additional interesting data already published [*Hubble Space Telescope* (HST), *Spitzer*, etc.] (six objects) and/or evidence for perturbed nuclear kinematics [full width at half-maximum (FWHM) of the forbidden lines $> 800 \text{ km s}^{-1}$] based on optical SDSS emission-line spectrum (six objects). We indicate in the last column of Table 1 which of these additional criteria were applied for each object. ‘IS’, ‘OD’ and ‘PK’ mean ‘interacting system’, ‘other data’ and ‘perturbed kinematics’ respectively. A ‘–’ in that column means that no additional criteria were applied, apart from the three mentioned above, which were common to all objects. The selection criteria applied by other authors in their programmes are unknown. Therefore, our sample is likely to be affected by different biases, and the results obtained with our work cannot be extrapolated to the general population of optically selected type 2 quasars.

The observing programme consisted of obtaining for each object a continuum+emission line image followed by long-slit

Table 1. Summary of the observations. The redshift z (column 2) is the value measured with the FORS2 spectra. The filter used for the intermediate- or narrow-band images is shown in column 4 for those objects for which a continuum+emission line image exists. The emission line within the filter spectral window is indicated in brackets. The GRIS_600RI grism was used to obtain the spectra of all objects. The slit position angles (PAs) measured north to east are shown in column 5. The exposure time in seconds appears in column 6. The seeing FWHM values (column 7) for each object were measured with several stars in the images of that specific object. The spatial scale per arcsec at the corresponding z is given in column 8. Column 9 shows specific criteria used for the selection of the objects (see text). ‘IS’, ‘OD’ and ‘PK’ mean ‘interacting system’, ‘other data’ and ‘perturbed kinematics’, respectively. The 2008 and 2009 runs are separated (upper and lower parts, respectively).

Object	z	Date	Filter/ grism	Slit PA	t_{exp} (s)	Seeing FWHM (arcsec)	arcsec kpc $^{-1}$	Selection criteria
SDSS J235818.87−000919.5	0.402	08/09/08	FILT_691_55+69 ([O III])		4×200	0.69 ± 0.07	5.34	IS, OD
			GRIS_600RI	60	6×700			
			GRIS_600RI	83	1×700			
SDSS J002531.46−104022.2	0.303	08/09/08	FILT_485_37+68 ([O II])		3×200	0.79 ± 0.02	4.45	OD
		08/09/08	GRIS_600RI	60	3×300	0.69 ± 0.02		
		09/09/08	GRIS_600RI	0	4×700			
SDSS J021758.19−001302.7	0.344	09/09/08	[S II]+62 ([O III])		4×200	0.69 ± 0.02	4.85	PK, OD
			V _{bess}		4×120			
			GRIS_600RI	116	4×700			
SDSS J023411.77−074538.4	0.310	09/09/08	H α +83 ([O III])		4×200	0.67 ± 0.04	4.52	PK
			GRIS_600RI	171	4×700			
SDSS J084943.82+015058.2	0.375	18/04/09	GRIS_600RI	153	2×700	0.88 ± 0.08	5.13	–
		18/04/09	GRIS_600RI	65.5	4×700			
SDSS J095514.11+034654.2	0.422	17/04/09	GRIS_600RI	115	6×700	1.60 ± 0.04	5.52	PK
SDSS J115314.36+032658.6	0.575	18/04/09	GRIS_600RI	65	6×700	0.8 ± 0.1	6.53	–
SDSS J122845.74+005018.7	0.575	17/04/09	GRIS_600RI	170	6×700	1.6 ± 0.1	6.54	PK
SDSS J130740.56−021455.3	0.425	18/04/09	GRIS_600RI	76	6×700	0.83 ± 0.03	5.54	PK
SDSS J133735.02−012815.7	0.329	17/04/09	GRIS_600RI	159	6×700	1.47 ± 0.09	5.60	OD, PK
SDSS J140740.06+021748.3	0.309	18/04/09	GRIS_600RI	150	4×700	0.73 ± 0.04	4.52	OD
SDSS J141315.31−014221.0	0.380	18/04/09	GRIS_600RI	45	6×700	1.54 ± 0.09	5.18	OD
SDSS J154613.27−000513.5	0.383	18/04/09	GRIS_600RI	109	6×700	0.90 ± 0.05	5.20	–

spectroscopy. Besides the interest of their scientific content, the goal of obtaining these images was to identify extended ionized nebulae (EINe) and/or other interesting gaseous features such as tidal tails, compact knots, etc. which helped to decide how to place the spectroscopic slit.

Unfortunately, due to technical problems at the observatory such deep continuum+emission line images could only be obtained during the 2008 run (i.e. for four objects) and only shallow continuum images are available for the 2009 run (nine objects). As a consequence, we did not have prior information about the possible existence of extended diffuse emission-line structures and their morphology for most objects observed during this run. The continuum images were not deep enough in general either to look for interesting features such as tidal tails, bridges, etc. So, the spectroscopic slit had to be placed blindly or through continuum sources near the quasar in the image, with the goal of checking their z .

All spectra were obtained with the 600RI+19 grism and the GG435+81 order sorting filter. The useful spectral range was $\sim 5030\text{--}8250 \text{ \AA}$ in the 2008 run and $\sim 5300\text{--}8600 \text{ \AA}$ in the 2009 run, so that in all cases at least the H β and [O III] $\lambda\lambda 4959, 5007$ lines were within the observed spectral range. The imaging and spectroscopic data reduction process is described in Villar-Martín et al. (2010). The pixel scales are $0.25 \text{ arcsec pixel}^{-1}$ and $0.83 \text{ \AA pixel}^{-1}$ in the spatial and spectral directions, respectively. The spectral resolution, as measured from the sky emission lines, was FWHM =

7.2 ± 0.2 and $5.4 \pm 0.2 \text{ \AA}$ for the 2008 and 2009 runs, respectively. The slit width was 1.3 arcsec in 2008 and 1.0 arcsec in 2009.

The log of the observations is shown in Table 1. The seeing size was measured for each object using several stars in the image. Comparison of several spectrophotometric standard stars taken with a 5-arcsec slit during the run gave a flux calibration accuracy of 5 per cent over the entire spectral range.

Using the spectra of several standard stars, geometric distortion was found to be $< 2 \text{ pixel}$ (0.5 arcsec) across the entire spectral range in all cases, with different values for different stars. In order to correct for this effect for each quasar, observations of a bright star with a similar telescope position would be required. Since these are not available and given the small magnitude of the distortion, we decided not to apply any correction (the quasar continuum cannot be used for this purpose, because the continuum spatial centroid at different wavelengths can change for various reasons such as reddening). We were careful when extracting the spectra from different apertures for a given object to make sure that such distortion did not have any negative impact on the analysis.

To perform the spectroscopic analysis, the line profiles were fitted with Gaussian functions (one or more, depending on the quality of the fit). The FWHM values were corrected for instrumental broadening in quadrature ($\text{FWHM} = 7.2 \pm 0.2 \text{ \AA}$ or $5.4 \pm 0.2 \text{ \AA}$ depending on the observing run). Slit effects could be present specially during the 2008 run, since point sources did not fill the slit (seeing

FWHM = 0.65 ± 0.05 arcsec versus 1.3-arcsec slit). We do not expect this to affect the conclusions presented in this paper.

3 ANALYSIS AND RESULTS

The results of the imaging and spectroscopic analysis are presented in this section.

Several considerations must be taken into account. One of the studies we perform here is the characterization of the gas ionization properties with the goal of exploring the nature of the excitation mechanism at different spatial locations for each quasar (stellar versus AGN photoionization, i.e. ionization by the continuum emitted by the quasar). The diagnostic diagram $[\text{O III}]\lambda 5007/\text{H}\beta$ versus $[\text{O II}]\lambda 3727/\text{H}\beta$ is used for this purpose. We chose this diagram because it involves the strongest lines detected in the spectra of most spatial locations under consideration, and because they provide useful information about the presence of both AGN and/or stellar photoionization. Diagnostic diagrams will be shown only for objects with $[\text{O II}]$ within the observed spectral range and with detected extended emission-line structures.

The data will be compared with predictions from the standard photoionization model sequence (Robinson et al. 1987) often applied to low and high redshift type 2 AGNs (see Villar-Martín et al. 2008, 2010, for a discussion about its application to type 2 quasars). The models assume solar metallicity, gas density $n = 100 \text{ cm}^{-3}$ and power-law index $\alpha = -1.5$. Reddening is ignored. The ionization parameter U varies along the sequence¹ [models with $\log(U) = -3, -2$ and -1 are marked in each diagram]. The assumption of this n value is supported by measurements of EELR densities associated with type 1 quasars in the range \sim several tens to several hundred cm^{-3} (e.g. Fu & Stockton 2008). The existence of densities as high as 10^6 cm^{-3} in the narrow-line region (NLR) is not discarded, but the large strength of the $[\text{O II}]\lambda 3727$ line, which has a critical density of $\sim 3 \times 10^3 \text{ cm}^{-3}$, suggests that the line fluxes have a very high contribution of much lower density gas. In addition, varying the gas density between several cm^{-3} and $<3000 \text{ cm}^{-3}$ is equivalent to varying the ionization parameter U , which is accounted for in the models.

The locations of the H II galaxies from the catalogue by Terlevich et al. (1991) are also shown for comparison.

The interpretation of the results based on these diagnostic diagrams must be considered with caution, since they do not allow an unambiguous discrimination between stellar and AGN photoionization. Other ratios such as $[\text{N II}]\lambda 6583/\text{H}\alpha$ or $[\text{S II}]\lambda \lambda 6716, 6731/\text{H}\alpha$ would be needed, but they are outside the spectral range covered by our data.

Type 2 AGNs in general and type 2 quasars in particular present a large scatter in this and other diagnostic diagrams (e.g. Lamareille et al. 2004; Villar-Martín et al. 2008), with a substantial fraction overlapping with H II galaxies. Marked differences in the location of the spectra (e.g. location in the AGN area versus the H II galaxy area) have been usually interpreted as a consequence of a range of gas and/or AGN ionizing continuum properties. Villar-Martín et al. (2008) showed that the additional contribution of stellar photoionization, which has generally been ignored, can be an alternative explanation. We will use other information such as the spatial morphology and line kinematic properties of the ionized gas to try to

disentangle between both scenarios: stellar versus AGN photoionization.

Dust extinction has been taken into account whenever possible (Osterbrock 1989), since it could have an impact on the interpretation of the line ratios.

The effects on the measured fluxes of some lines due to the absorption features on the underlying host galaxy continuum are expected to be negligible for most objects in the sample, due to the large equivalent widths of the emission lines. For those few objects where this effect could be relevant, the impact on the interpretation of the line ratios will be discussed. We have not subtracted the underlying galaxy continuum because the uncertainty on determining the continuum level introduces larger errors on the measured line fluxes than if the original spectra are used. The conclusions of our work are not affected by this.

As in other studies of EELRs associated with quasars and radio galaxies, we define EELRs as spatially extended regions of ionized gas associated with the quasars, rather than with companion objects (e.g. the ionized gas of a companion nucleus/galaxy/knot is not considered part of an EELR). This definition is independent of gas excitation mechanism, the nature and the origin of the nebulae. Thus, features such as ionized tidal tails/bridges are included in the concept of EELR. When an extended nebula of a different or unknown nature is found associated with a quasar, we will refer to it as the quasar-ionized nebula (ionization cones, for instance).

The nuclear spectra and the nuclear line ratios for all objects are shown in Fig. 1 and Tables 2 and 3, respectively. The electron temperatures have been measured using the $[\text{O III}]\lambda \lambda 5007, 4959$ and $[\text{O III}]\lambda 4363$ lines (Osterbrock 1989).

Hereafter, $[\text{O III}]$, $[\text{O II}]$, He II will be used instead of $[\text{O III}]\lambda 5007$, $[\text{O II}]\lambda 3727$ and $\text{He II}\lambda 4686$.

3.1 SDSS J2358–00 ($z = 0.402$)

This quasar is a member of an interacting system (Fig. 2; see also Zakamska et al. 2006). A tidal tail stretches from the companion nucleus (nuc2 in the figure) to the west and apparently joins it with another companion located at ~ 15 arcsec or 80 kpc in projection, although the z for this object is unknown. Low SB diffuse extended emission is detected in a larger area south of the quasar and the companion nucleus. A knot is located at ~ 5.5 arcsec or 30 kpc east of the quasar. It is elongated in the east–west (EW) direction.

The 2D spectra of the $\text{H}\beta$ – $[\text{O III}]$ spectral region for both slit position angles (PAs) are shown in Fig. 3. PA 60 goes through the quasar and the companion nucleus nuc2, which emits both continuum and strong emission lines. PA 83 goes through the quasar nucleus and the knot. Low SB, diffuse extended $[\text{O III}]$ emission is detected at both sides of the continuum centroid along both PAs for total extensions of 7.5 arcsec or 40 kpc along PA 60 and 12 arcsec or 64 kpc along PA 83.

Several apertures were used to extract 1D spectra from different spatial regions along both slits, which are also shown in Fig. 2. The locations of the line ratios measured for the individual spectra are shown in the diagnostic diagrams in the same figure. The quasar nuclear line ratios both corrected (green solid circle) and uncorrected (dark blue solid circle) for dust reddening and the ratios of the adjacent spatial regions (cyan symbols) are successfully explained by AGN photoionization along both PAs.

On the contrary, the spectrum of the companion (nuc2) shows very low line ratios, noticeably lower than those measured in typical type 2 AGNs. Similar values are often measured in H II galaxies (e.g. Lamareille et al. 2004). Dust reddening could shift an AGN

¹ $U = Q/4\pi r^2 nc$, where Q is the quasar photon ionizing luminosity, r is the radial distance to the ionizing source, n is the gas density and c is the speed of light.

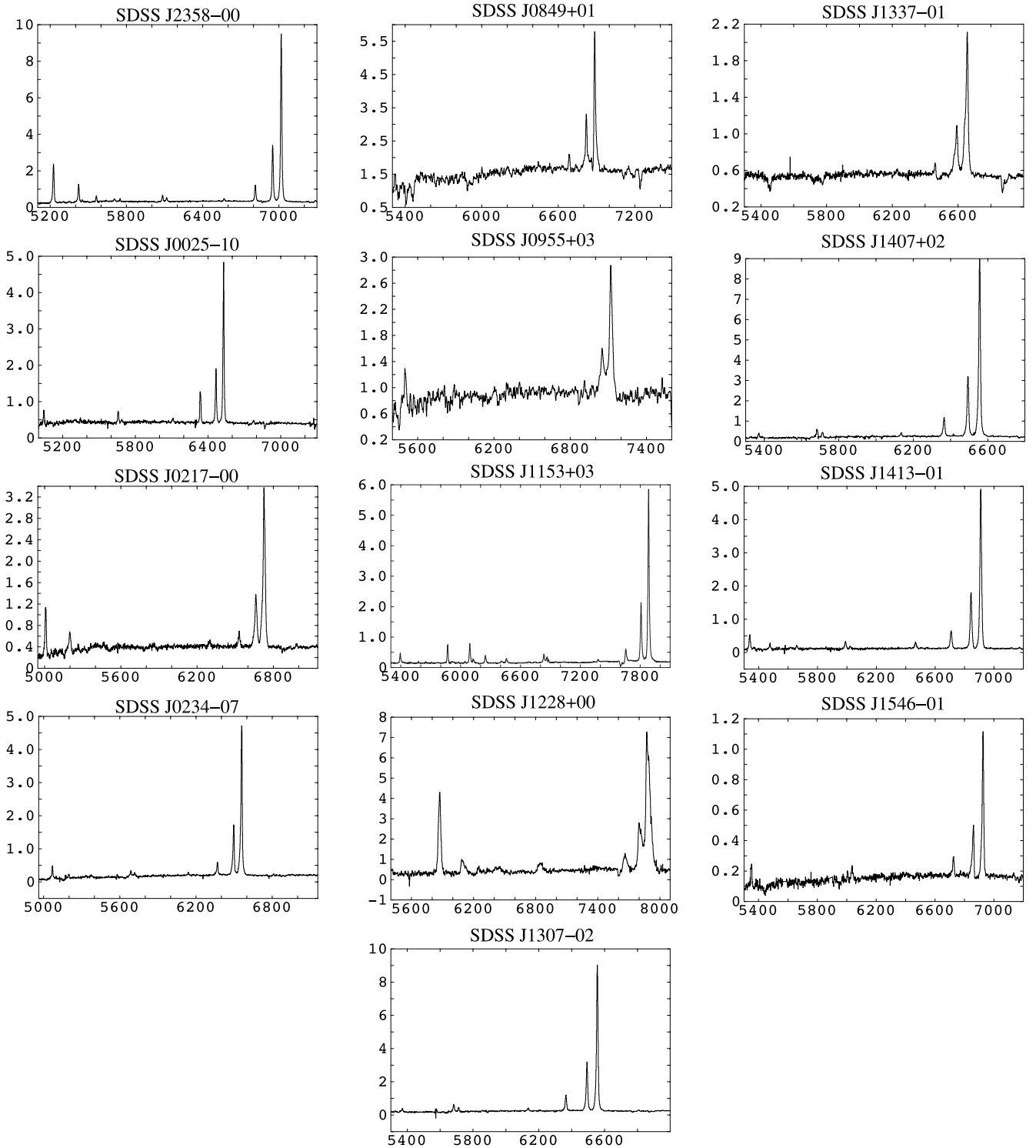


Figure 1. Nuclear spectra of the quasars studied in this work. The flux is given in units of $10^{-16} \text{ erg s}^{-1} \text{ cm}^{-2}$ and the wavelength in \AA in all cases except for SDSS J0849+01, SDSS J0955+03, SDSS J1228+00 and SDSS J156-00 where the flux factor is 10^{-17} . The strongest line in the blue is $[\text{O II}]\lambda 3727$. $\text{H}\beta$ and $[\text{O III}]\lambda\lambda 4959, 5007$ are clearly identified at the reddest wavelengths.

to the H II galaxy region in the diagram, since the $[\text{O II}]/\text{H}\beta$ would be observed to be lower, while $[\text{O III}]/\text{H}\beta$ would be similar. It is not possible to estimate the reddening from the Balmer emission lines, because the nuc2 spectrum is noisy. However, the very low $[\text{O III}]/\text{H}\beta = 0.5 \pm 0.1$ is more suggestive of H II galaxies than type 2 AGNs. Moreover, its emission lines are very narrow ($\text{FWHM} \lesssim$

150 km s^{-1}) compared with typical values of type 2 AGNs (several hundred km s^{-1}). Both properties suggest that this is the actively star-forming nucleus of a companion galaxy. The shift in velocity relative to the quasar is $+300 \pm 80 \text{ km s}^{-1}$ (this error takes into account slit effect uncertainties, see Section 2). This is within the range expected for merging system ($\lesssim \text{few hundred km s}^{-1}$).

Table 2. Nuclear line ratios relative to $H\beta$ for the quasars observed in the 2008 run. The ratios corrected for dust extinction are based on the reddening derived from $H\gamma/H\beta$ (case B recombination value is 0.47). The $H\beta$ flux is given in units of $10^{-16} \text{ erg s}^{-1} \text{ cm}^{-2}$. T_4 is the electronic temperature in units of 10^4 K .

Line/ $H\beta$	0217–00 Observed	0217–00 ^a Dered.	2358–00 Observed	2358–00 Dered.	0234–07 Observed	0234–07 Dered.	0025–10 Observed	0025–10 Dered.
[O II]	1.9 ± 0.3	17 ± 11	2.52 ± 0.08	4.7 ± 0.2	N/A	N/A	N/A	N/A
[Ne III] λ 3869	0.93 ± 0.15	6.6 ± 4	0.97 ± 0.04	1.71 ± 0.08	0.8 ± 0.1	1.2 ± 0.3	0.32 ± 0.03	0.60 ± 0.09
[O III] λ 4363	0.18 ± 0.03	0.50 ± 0.18	0.21 ± 0.02	0.28 ± 0.03	0.26 ± 0.04	0.32 ± 0.05	0.09 ± 0.02	0.13 ± 0.01
He II	0.36 ± 0.06	0.5 ± 0.1	0.15 ± 0.01	0.17 ± 0.01	0.20 ± 0.02	0.22 ± 0.02	0.11 ± 0.01	0.13 ± 0.01
[O III] λ 5007	14.6 ± 2.3	11 ± 2	10.9 ± 0.4	9.9 ± 0.4	12.6 ± 0.6	11.8 ± 0.7	4.6 ± 0.2	4.2 ± 0.2
T_4	1.2 ± 0.1	2.5 ± 0.7	1.5 ± 0.1	1.8 ± 0.1	1.5 ± 0.1	1.78 ± 0.16	1.51 ± 0.15	1.9 ± 0.1
$H\gamma$	0.17 ± 0.05	0.47	0.35 ± 0.02	0.47	0.38 ± 0.04	0.47	0.34 ± 0.02	0.47
H δ	No	No	0.15 ± 0.03	0.23 ± 0.05	0.17 ± 0.05	0.23 ± 0.08	0.13 ± 0.03	0.21 ± 0.05
$F(H\beta)$	4.5 ± 0.6		10.6 ± 0.3		5.3 ± 0.2		10.7 ± 0.5	

^aThe reddening values estimated for 0217–00 are uncertain possibly due to underlying stellar absorption (see Section 3.3).

Table 3. Nuclear line ratios relative to $H\beta$ for the objects observed in the 2009 run. When the reddening was negligible (1153+03, 1228+00) or uncertain (0849+01, 0955+01, 1337–01, 1546–00), no dereddened line ratios are shown. N/A means that the line was outside the spectral range or, in the case of T_4 , that the calculation could not be done due to the non-detection of [O III] λ 4363. ‘No’ means the line was not detected or too noisy.

Line/ $H\beta$	0849+01 Observed	0955+03 Observed	1153+03 Observed	1228+00 Observed	1307–02 Observed	1307–02 Dered.
[O II]	N/A	N/A	0.8 ± 0.1	4.0 ± 0.6	1.96 ± 0.08	2.5 ± 0.3
[Ne III] λ 3869	1.4 ± 0.4	2.0 ± 0.8	0.9 ± 0.1	0.9 ± 0.1	0.75 ± 0.04	0.9 ± 0.1
[O III] λ 4363	No	No	0.35 ± 0.04	0.15 ± 0.10	0.15 ± 0.01	0.17 ± 0.02
He II	0.37 ± 0.08	No	0.12 ± 0.02	No	0.38 ± 0.02	0.40 ± 0.02
[O III] λ 5007	12 ± 1.5	16 ± 4	14.1 ± 0.09	12 ± 1	10.9 ± 0.3	10.5 ± 0.3
T_4	N/A	N/A	1.7 ± 0.1	1.25 ± 0.35	1.30 ± 0.05	1.39 ± 0.07
$H\gamma$	No	No	0.47 ± 0.06	0.6 ± 0.1	0.42 ± 0.02	0.47
H δ	No	No	0.25 ± 0.03	0.24 ± 0.05	0.21 ± 0.02	0.25 ± 0.03
$F(H\beta)$	0.52 ± 0.06	4 ± 1	9.6 ± 1.0	2.8 ± 0.3	4.51 ± 0.09	7.0 ± 1.5
Line/ $H\beta$	1337–01 ^a Observed	1407+02 Observed	1407+02 Dered.	1413–01 Observed	1413–01 Dered.	1546–00 Observed
[O II]	N/A	N/A	N/A	N/A	N/A	N/A
[Ne III] λ 3869	N/A	N/A	N/A	0.61 ± 0.03	0.92 ± 0.07	1.1 ± 0.2
[O III] λ 4363	0.6 ± 0.1	0.25 ± 0.01	0.30 ± 0.02	0.14 ± 0.02	0.17 ± 0.03	0.7 ± 0.1
He II	0.8 ± 0.1	0.18 ± 0.01	0.19 ± 0.01	0.33 ± 0.1	0.50 ± 0.03	No
[O III] λ 5007	25 ± 2	10.9 ± 0.4	10.3 ± 0.4	9.6 ± 0.4	9.0 ± 0.4	8.3 ± 0.9
T_4	1.7 ± 0.2	1.64 ± 0.07	1.85 ± 0.08	1.33 ± 0.08	1.5 ± 0.1	4.5 ± 1.0
$H\gamma$	No	0.39 ± 0.02	0.47	0.38 ± 0.01	0.47	No
H δ	No	0.19 ± 0.04	0.25 ± 0.05	0.19 ± 0.03	0.26 ± 0.24	No
$F(H\beta)$	1.28 ± 0.08	10.1 ± 0.2	25 ± 4	75 ± 3	170 ± 13	1.6 ± 0.2

^aThe $H\beta$ flux of SDSS 1337–01 is affected by underlying stellar absorption (see Section 3.10).

Both continuum and line emission are detected at the location of the knot and at the same z as the quasar. The spectrum is rather noisy and $H\beta$ is not detected. We can only say that the location in the diagnostic diagrams (Fig. 3, bottom) using the $H\beta$ flux upper limits overlaps with the H II galaxies area and lies far from the standard AGN sequence.

The knot looks sharper in the image than it does in the long-slit spectrum (see Figs 2 and 3). This and the similar ratios between the fluxes of the knot and the stars in the intermediate and the broad-band images suggest that it is dominated by continuum emission. This feature appears very prominently in the rest-frame V-band Advanced Camera for Surveys (ACS) *HST* image (Zakamska et al. 2006). It shows knotty internal substructure and seems to be a part of the complex system of knots and filaments associated with the quasar. This confirms that the knot belongs to the quasar system.

Based on these results, we propose that SDSS J2358–00 is interacting with a companion star-forming galaxy whose nuclear gas is photoionized by young stars possibly formed as a consequence of the interaction. The quasar is associated with an EIN of maximum extension $\sim 64 \text{ kpc}$. The nuclear gas and the extended adjacent gaseous regions are preferentially photoionized by the quasar.

3.2 SDSS J0025–10 ($z = 0.303$)

The VLT-FORS2 images of this quasar show two nuclei (one hosts the quasar) separated in projection by 1.1 arcsec or $\sim 5 \text{ kpc}$ and two tidal tails extending north and south (Fig. 4). These are clear signatures of an ongoing merger. Two knots are also detected to the east (knot1 in the figure) and to the west (knot2). knot1 appears much more prominently in the intermediate-band image, which contains

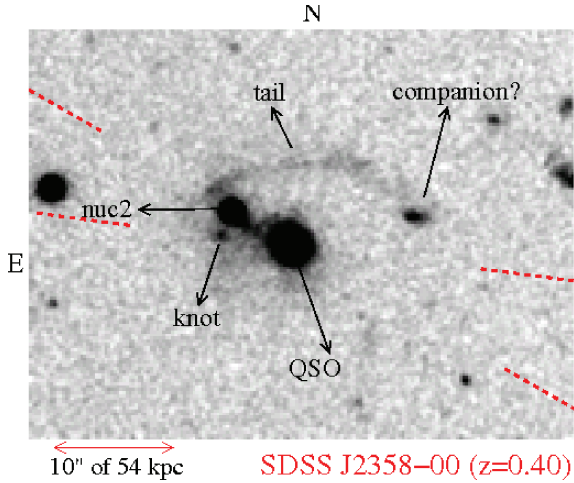


Figure 2. FORS2+VLT intermediate-band image of SDSS J2358–00 containing the [O III] line. The original image has been boxcar smoothed with a 2×2 window. The quasar is a member of an interacting system. A spectacular tidal tail stretches to the E apparently joining the companion nucleus (nuc2) with another galaxy. The knot identified in the figure is probably at the same z (see text). The location of the PA 60 and 83 slits used to obtain the long-slit spectra are indicated with red dashed lines.

the [O II] line, while it is undetected in the broad-band image. This suggests knot1 is an emission-line object at similar z as the quasar. Its compact appearance is reminiscent of a star-forming knot. The opposite happens with knot2. It appears much more prominently relative to other features in the broad-band image and thus it is most probably a continuum source of unknown z .

We show in Fig. 5 the $H\beta$ –[O III] 2D spectra for the two slit PAs. PA 0 goes through the quasar and the northern tidal tail (tail1), and PA 60 goes through the quasar nucleus and the nucleus of the companion (nuc2, Fig. 4). The visual inspection of both spectra shows that the tidal tail and the companion nucleus emit strong continuum and emission lines, which are much narrower than those of the quasar. nuc2 presents a shift in velocity relative to the quasar of $0 \pm 70 \text{ km s}^{-1}$ (slit effects are also accounted for, see Section 2). The velocity blueshift of the tidal tail relative to the quasar is also small ($-15 \pm 70 \text{ km s}^{-1}$).

The [O II] line was outside the observed spectral range and no diagnostic diagram is presented. The detection of strong He II (Table 2) is consistent with values measured in type 2 AGNs, which implies that AGN photoionization is the dominant mechanisms responsible for the ionization of the nuclear gas. This is further confirmed by the detection of [Ne V] $\lambda 3426$ in the SDSS spectrum. This, as for the rest of the sample, is to be expected since one of the selection criteria applied by Zakamska et al. (2003) was an emission-line spectrum typical of type 2 AGNs.

The spectra of the companion nucleus and the tidal tail are more reminiscent of H II galaxies than AGNs (see Fig. 5, bottom). The [O III]/ $H\beta$ values (1.26 ± 0.02 and 1.17 ± 0.08 , respectively) are very low compared with typical type 2 AGNs and similar to values frequently measured in H II galaxies (e.g. Lamareille et al. 2004). He II is undetected in nuc2 and the tidal tail, with $\text{He II}/H\beta < 0.02$ and < 0.05 , respectively. These low values are consistent with H II galaxies and smaller than ratios measured for typical type 2 AGNs (usually > 0.1 ; e.g. Robinson et al. 1987).

The emission lines are narrower in the tidal tail and nuc2 than at the quasar nucleus. $\text{FWHM}[\text{O III}] = 330 \pm 10 \text{ km s}^{-1}$ and $\text{FWHM}(H\beta) \leq 140 \text{ km s}^{-1}$ for nuc2; $\text{FWHM}[\text{O III}] = 310 \pm$

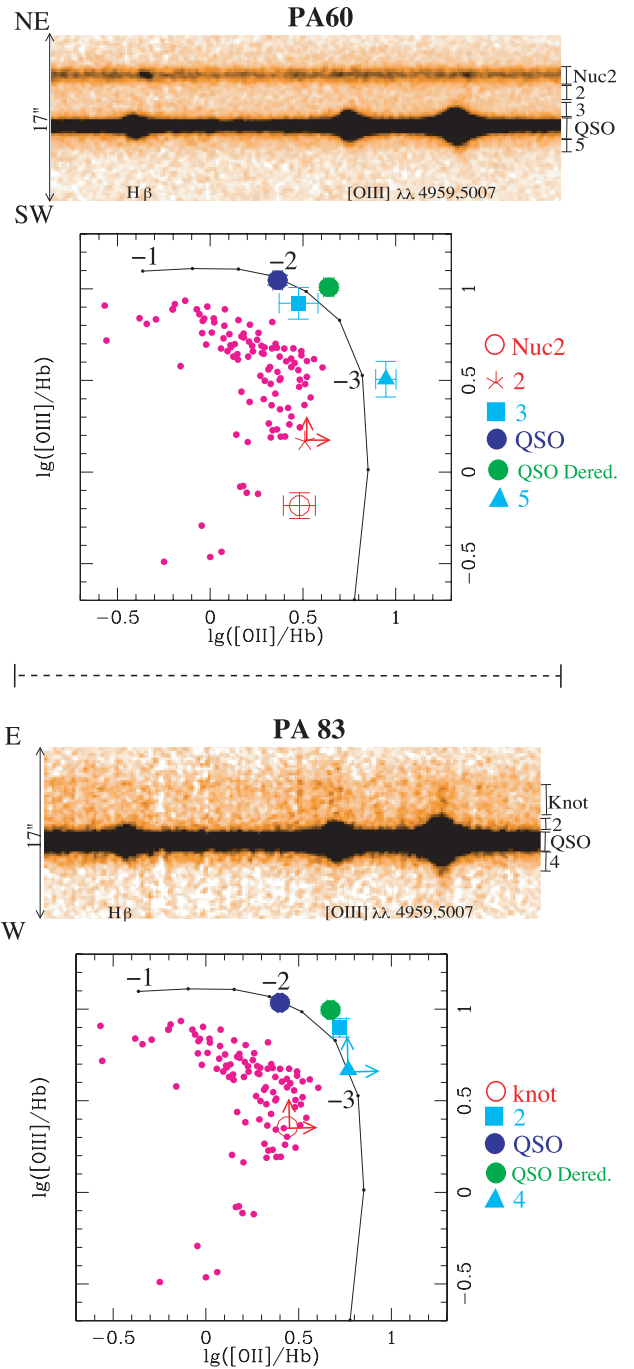


Figure 3. SDSS J2358–00. The $H\beta$ –[O III] 2D spectra along PA 60 and PA 83 are shown. The apertures used to extract 1D spectra of different spatial regions are indicated. Both spectra have been boxcar smoothed with a 2×2 window. In the diagnostic diagrams, the continuous black line represents the standard sequence of type 2 AGN photoionization models (see text). The ionization parameter varies along the sequence. $\log(U)$ values -1 , -2 and -3 are indicated. The small magenta symbols are the H II galaxies from Terlevich et al. (1991) catalogue. The line ratios for the individual spectra are shown on the corresponding diagnostic diagram. The quasar nuclear line ratios corrected (green solid circle) and uncorrected (blue solid circle) for reddening, as well as the ratios of the adjacent regions (cyan symbols), are successfully explained by the standard AGN photoionization models along both slit positions. The low values of the line ratios for the companion galaxy nucleus (nuc2, top diagnostic diagram) are more consistent with H II galaxies.

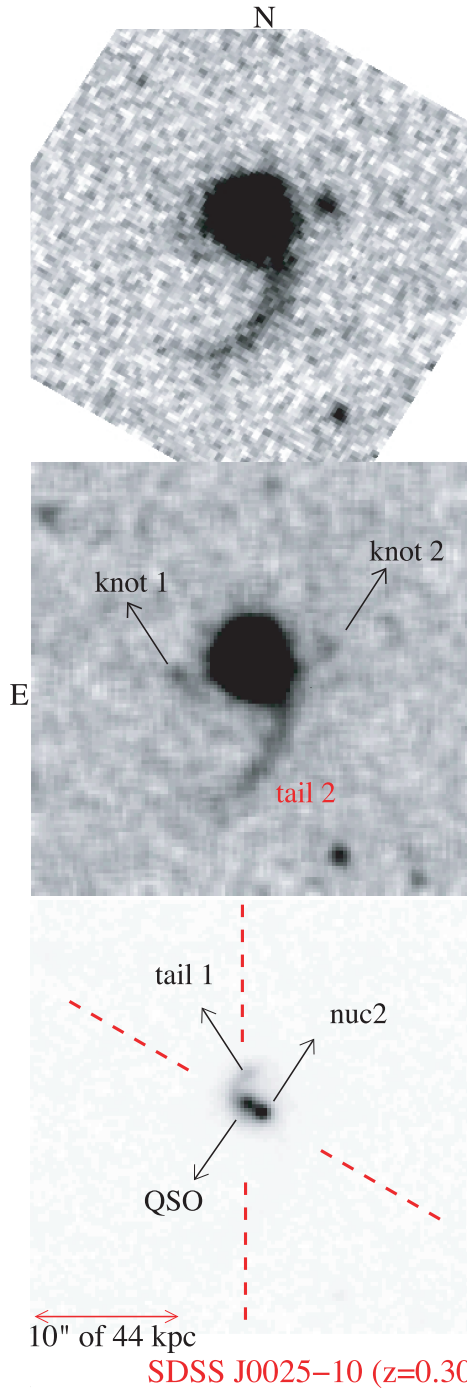


Figure 4. Top panel: FORS2+VLT V-Bess broad-band image of SDSS J0025–10, boxcar smoothed with a 2×2 window. Middle and bottom panels: intermediate-band image containing the [O II] line, shown with two different contrasts to highlight the faint (middle, boxcar smoothed with a 2×2 window) and bright (bottom, non-smoothed) features. The double nucleus and tidal tails are clear signatures of an ongoing merger. The PA 0 and PA 60 slits are indicated with red dashed lines.

30 km s^{-1} and $\text{FWHM}(\text{H}\beta) \leq 140 \text{ km s}^{-1}$ for the tidal tail. The quasar nucleus shows $\text{FWHM} = 400 \pm 40 \text{ km s}^{-1}$ and 380 ± 20 for [O III] and $\text{H}\beta$, respectively.

Thus, SDSS J0025–10 is undergoing a merger process with a companion star-forming galaxy. We propose that both the companion nucleus and the northern tidal tail are photoionized by young

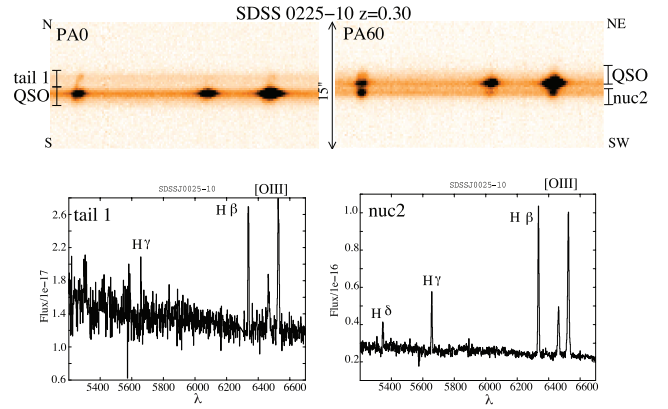


Figure 5. SDSS J0025–00. The spectral properties of the tidal tail and the companion nucleus (nuc2) are typical of H II galaxies/regions.

stars which have probably formed as a consequence of the interaction process. knot1 is probably a companion star-forming object. We find no clear evidence for a quasar EIN along PA 0 or PA 60 at SB levels $\gtrsim 3\sigma = 3.2 \times 10^{-18} \text{ erg s}^{-1} \text{ cm}^{-2} \text{ arcsec}^{-2}$.

3.3 SDSS J0217–00 ($z = 0.344$)

The VLT-FORS2 broad- and narrow-band images are shown in Fig. 6. An extended diffuse structure is detected towards the north-west (NW), whose morphology appears more clearly defined in the broad-band image and is reminiscent of a tidal tail. A compact knot is also detected to the east, which appears relatively stronger in the narrow-band image. This suggests that it is a strong line emitter at the same z as the quasar.

The PA 116 slit crosses both the tidal tail and the knot. The $\text{H}\beta$ –[O III] 2D spectrum (Fig. 7) shows that the compact knot emits strong lines and very faint continuum, as expected from the images. Low SB lines are also detected between the quasar and the knot, possibly emitted by an EIN associated with the quasar. The structure reminiscent of a tidal tail mentioned above emits only faint, diffuse continuum.

The nuclear line ratios are shown in Table 2. The reddening derived from the Balmer lines is most likely wrong, since the galaxy continuum is strong and $\text{H}\gamma$ and $\text{H}\delta$ (not so much $\text{H}\beta$, which has larger equivalent width) are likely to be strongly absorbed. Given the large uncertainties due to this effect, we will ignore nuclear dust reddening in the diagnostic diagram in this case. The knot is dominated by line emission and is not affected by this problem: $\text{H}\gamma/\text{H}\beta = 0.46 \pm 0.03$ is consistent with the case B recombination value 0.47 (Osterbrock 1989). It is therefore not reddened.

Three apertures were used to extract 1D spectra from different spatial regions along the slit (Fig. 7, top): the knot, the quasar and the intermediate region between them. The locations of the individual spectra are shown in the diagnostic diagram. While the nuclear spectrum lies very far from the H II galaxies and is consistent with the AGN models (also He II is strong, $\text{He II}/\text{H}\beta = 0.36 \pm 0.06$; Table 2), the knot overlaps with the H II galaxy region. For the intermediate region, lower limits are shown, due to the non-detection of $\text{H}\beta$. The location overlaps with the H II galaxy region as well.

The lines emitted by the knot are split into two kinematics components (see Fig. 7, top). The dominant component is very narrow ($\text{FWHM} \lesssim 120 \text{ km s}^{-1}$) and shows very low $[\text{O III}]/\text{H}\beta = 3.6 \pm 0.3$. These properties and its location on the H II region area in the diagnostic diagrams suggest that the knot is a star-forming object

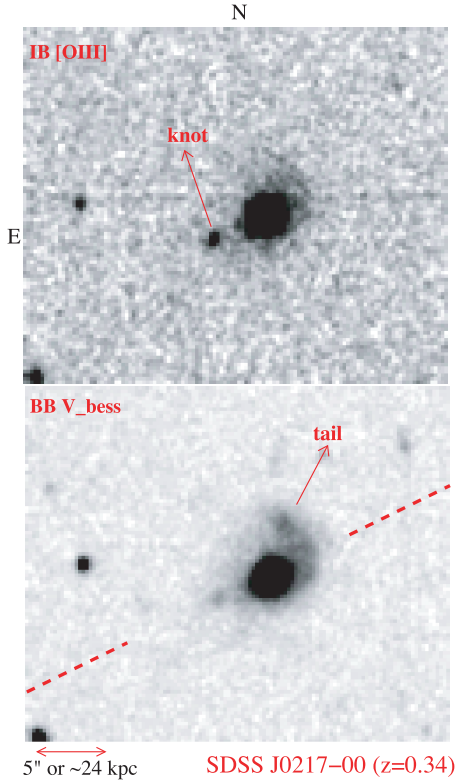


Figure 6. FORS2+VLT images of SDSS J0217–00. Top: narrow-band image containing the [O III] line. Bottom: V-bess broad-band image. Both have been boxcar smoothed with a 2×2 window. Different features appear with different prominence in the two images. The knot is much clearer in the narrow-band image, suggesting it is dominated by line emission, while the extended diffuse structure towards the NW is much more prominent in the broad-band image suggesting it emits mostly continuum. This appears like a clear tidal tail in the broad-band image. The location of the PA 116 slit is shown on the bottom panel.

where the gas is photoionized by young stars. It is redshifted by $-260 \pm 70 \text{ km s}^{-1}$ relative to the quasar (uncertainties due to slit effects have been taken into account). The faintest kinematic component is broader ($\text{FWHM} = 260 \pm 70$) and is more highly ionized ($[\text{O III}]/\text{H}\beta = 7.0 \pm 0.4$). It is possible that this is the extension of the intermediate ionized region detected between the quasar and the knot, which, as proposed above, could be an EIN associated with the quasar. This is supported by the spatial continuity observed for the [O III] line emission between this region and the fainter kinematic component of the knot along the slit.

Therefore, the morphology of SDSS J0217–00 is reminiscent of a galaxy with a continuum tidal tail which is a signature of an merger event. The quasar is associated with a companion star-forming knot where the gas is photoionized by the young stars. An EIN is detected across $\sim 4 \text{ arcsec}$ or 19 kpc between both objects and it might connect them physically.

3.4 SDSS0234–07 ($z = 0.310$)

No extended structures are detected in the broad- or the narrow-band images (Fig. 8) of this quasar. The faint object, marked as G1 in the figure, falls within the slit. The spectrum shows that it is a faint continuum source of unknown z .

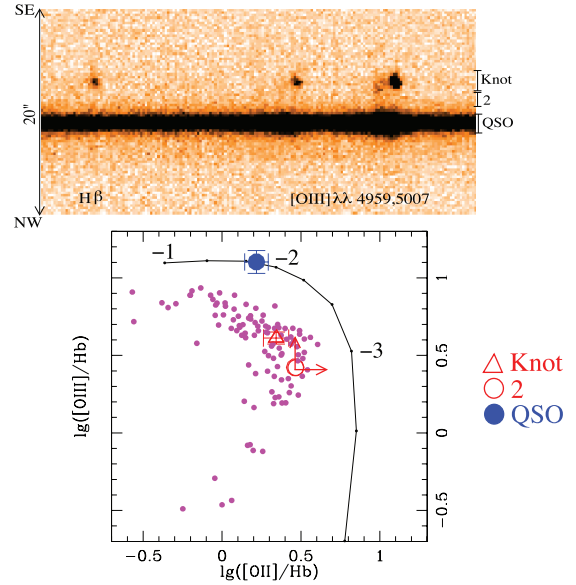


Figure 7. $\text{H}\beta$ –[O III] 2D spectrum of SDSS J0217–00 (top). The apertures used to extract 1D spectra of different spatial regions are indicated. The line ratios for the individual spectra are shown in the diagnostic diagram below. The quasar nuclear line ratios (blue solid circle) are successfully explained by the standard AGN photoionization models. The companion knot (open red triangle) overlaps with the region occupied by H II galaxies. Other symbols and lines as in Fig. 3.

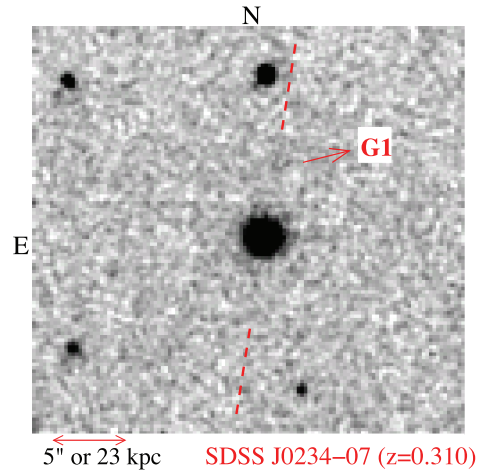


Figure 8. Narrow-band image of SDSS J0234–00 containing [O III]. The original image has been boxcar smoothed with a 2×2 window. The spectrum shows that G1 is a continuum source of unknown z .

The spatial profile of the [O III] line (Fig. 9) is dominated by a spatially unresolved component of $\text{FWHM} = 0.57 \pm 0.05 \text{ arcsec}$ (versus $0.67 \pm 0.04 \text{ arcsec}$ FWHM seeing measured on the images). There is no evidence for extended line emission along PA 171 associated with this quasar at SB levels $\gtrsim 3\sigma = 3.5 \times 10^{-18} \text{ erg s}^{-1} \text{ cm}^{-2} \text{ arcsec}^{-2}$.

The objects discussed below were observed during the 2009 run. As mentioned in Section 2, no narrow or intermediate emission line+continuum images are available. Therefore, except in two cases where the continuum-dominated images revealed or suggested a galaxy interaction or a peculiar quasar morphology, the slit was placed blindly or through objects near the quasar, with the goal of checking their z .

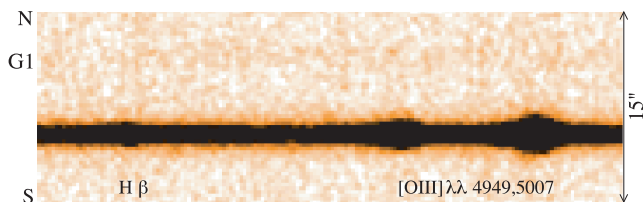


Figure 9. $H\beta$ -[O III] 2D spectrum of SDSS J0234-07. The original spectrum has been boxcar smoothed with a 2×2 window. There is no evidence for extended line emission along PA 171.

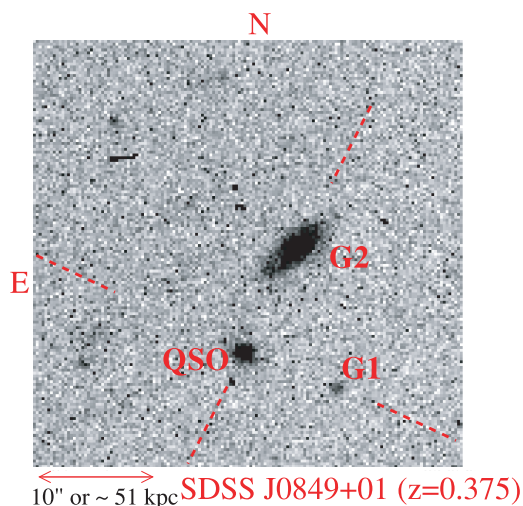


Figure 10. Narrow-band continuum image of SDSS J0849+01 (identified with quasi-stellar object, QSO). It was obtained with the $\text{He II } 6500+49$ FORS2 filter and covers the rest-frame spectral range $\sim 3450\text{--}3500 \text{ \AA}$. The slit PAs 153 and 65 were selected to include galaxies G1 and G2. Both are emission-line galaxies at $z = 0.950$ and 0.221 , respectively.

3.5 SDSS J0849+01 ($z = 0.376$)

The narrow-band continuum image is shown in Fig. 10. The emission-line galaxies G1 and G2 fall within the slits. G2 lies at $z = 0.221$. G1 emits a single emission line whose most likely identification is $[\text{O II}] \lambda 3727$ at $z = 0.950$ (rather than $\text{Ly}\alpha$ at $z = 4.98$), given the strong continuum emission bluewards of the line.

The spatial distribution of [O III] (Fig. 11) along PA 65 is dominated by a compact component which is successfully represented by a Gaussian function of $\text{FWHM} = 1.05 \pm 0.05 \text{ arcsec}$ (versus seeing $\text{FWHM} = 0.88 \pm 0.08$). Taking errors into account and possible seeing variations during the spectroscopic observations, it is not possible to discern whether the [O III] profile along PA 65 is spatially resolved. The emission lines are unresolved along PA 153 ($\text{FWHM} = 0.82 \pm 0.04 \text{ arcsec}$).

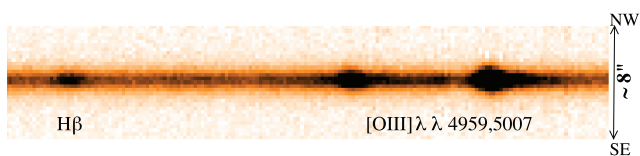


Figure 11. $H\beta$ -[O III] 2D spectrum of SDSS J0849+01. G1. There is no evidence for extended line emission along PA65, neither PA 153.

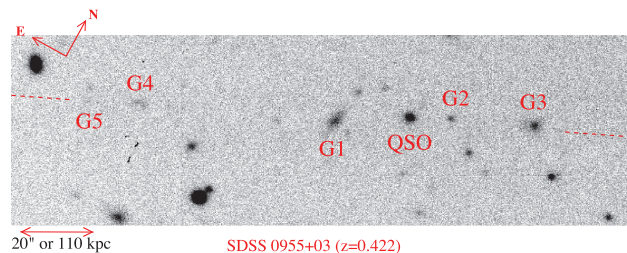


Figure 12. Broad-band image of SDSS J0955+03 (QSO in the image). It was obtained with the V_{High} FORS2 filter and covers the rest-frame spectral range $\sim 3470\text{--}4335 \text{ \AA}$. The slit was placed at PA 115, as marked by the dashed red line. G1, G2, G3, G4 and G5 fall within the slit. The spectra reveal they all are emission-line galaxies at different z , rather than the quasar.

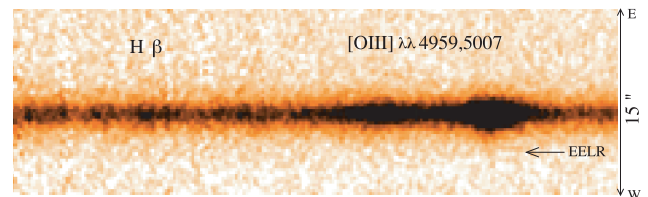


Figure 13. $H\beta$ -[O III] 2D spectrum of SDSS J0955+03. The original spectrum has been boxcar smoothed with a 2×2 window. Very faint extended emission is detected towards the west (indicated with ‘EELR’ in the figure.)

3.6 SDSS J0955+03 ($z = 0.422$)

The broad-band image is shown in Fig. 12. Several galaxies marked as G1, G2, G3, G4 and G5 in Fig. 9 fall within the slit. The spectra reveal that they are all emission-line galaxies at different z than the quasar.

The spatial profile of the emission lines along PA 115 (Fig. 13) is dominated by a barely resolved central component of $\text{FWHM} = 1.86 \pm 0.04 \text{ arcsec}$ (versus $1.60 \pm 0.04 \text{ arcsec}$). The seeing FWHM was very similar at the beginning and the end of this object exposures, so seeing variations during the spectroscopic observations are not likely to play a role, and the line emission is actually spatially extended. The implied intrinsic size is $\sim 1 \text{ arcsec}$ or $\sim 5.5 \text{ kpc}$. Given the strong contamination by the nuclear emission, it is not possible to isolate the emission from this EELR to analyse the kinematic and ionization properties. In addition, very faint emission is detected at $\sim 3\sigma$ level towards the west (indicated with ‘EELR’ in Fig. 13) up to a radial extent of 7 arcsec or 38.5 kpc from the continuum centroid.

3.7 SDSS J1153+03 ($z = 0.575$)

This quasar (Fig. 14) appears to be interacting with a companion galaxy (G1 in the figure), although a chance projection cannot be discarded from the image alone. The FORS2 slit was located at PA 65, crossing both nuclei.

The nuclear spectrum shows strong continuum compared with the other quasars in the sample and a very broad underlying $H\beta$ component (Fig. 15). The flux of this component has not been included in the $H\beta$ flux used to calculate the nuclear line ratios (Table 2). Broad underlying He II might also be present. Several $[\text{Fe VII}]$ emission lines are detected ($[\text{Fe VII}] \lambda 3586$, $[\text{Fe VII}] \lambda 3759$, $[\text{Fe VII}] \lambda 5159$). Forbidden high ionization lines (FHILs) have been detected in the spectra of many AGNs (e.g. Penston et al. 1984; Mullaney et al. 2009). Their ionization potential is $\gtrsim 100 \text{ eV}$ (99 eV for Fe^{+5}). Different works have suggested that they are emitted in an

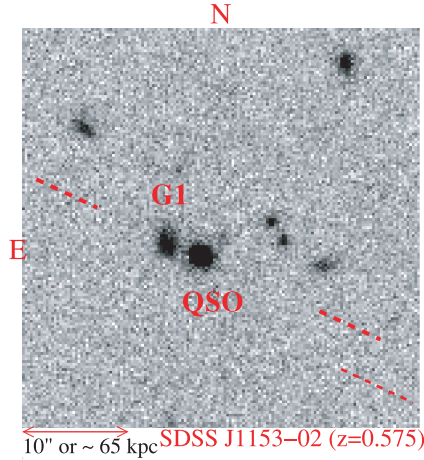


Figure 14. Narrow-band continuum image of SDSS J1153+03 (identified with QSO). It was obtained with the $H\alpha+83$ FORS2 filter, and it covers the rest-frame spectral range $\sim 4140\text{--}4185$ Å. The PA 65 slit is indicated. Galaxy G1 is at the same z as the quasar and they are probably interacting.

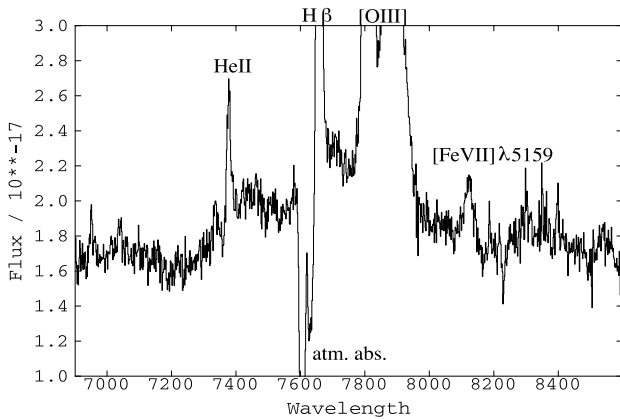


Figure 15. Very broad $H\beta$ is detected underneath the narrow emission lines (possibly very broad $HeII$ as well) in the nuclear spectrum of SDSS 1153+03. The deep absorption feature is produced by the atmosphere. $[FeVII]$ lines are also detected.

intermediate region between the NLR and the BLR (see Mullaney et al. 2009, for a review). More specifically, these authors propose that they are emitted by the illuminated face of the torus, a region with densities in the range $n \sim 10^5\text{--}10^{10}$ cm $^{-3}$. In SDSS J1153+03, as in other AGNs, the $[FeVII]$ lines are blueshifted relative to lower ionization forbidden lines such as $[OIII]$ and $[OII]$ by ~ 200 km s $^{-1}$ and $[FeVII]\lambda 5159$, the strongest line, is much broader than all other emission lines (~ 1200 km s $^{-1}$ versus several hundred km s $^{-1}$). The detection of strong continuum and very broad underlying $H\beta$ emission in the nuclear spectrum implies a viewing angle that allows to see not only the illuminated face of the torus, but also part of the broad line and continuum regions.

Fig. 16 shows the $H\beta$ - $[OIII]$ 2D spectrum. The quasar emission lines are clearly extended. $[OIII]$ extends across ~ 8 arcsec or 52 kpc. Line emission is detected at the location of galaxy G1 as well, but a more thorough analysis is required to disentangle whether the lines are emitted preferentially by the quasar EELR or G1. This is important, since one scenario or another will determine whether G1 is at similar z as the quasar.

The continuous and rather symmetric spatial distribution of the $[OIII]$ lines at both sides of the quasar suggests that they are

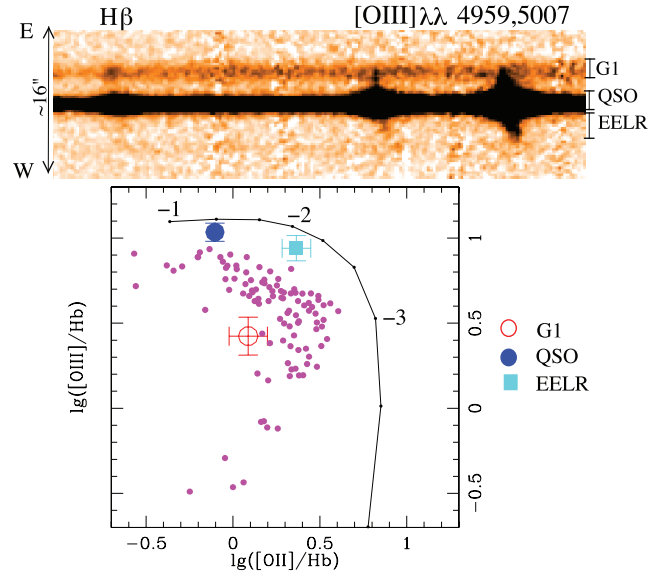


Figure 16. $H\beta$ - $[OIII]$ 2D spectrum of SDSS J1153+03 along PA 65 (top). The apertures used to extract the spectra of galaxy G1, the western EELR and the quasar are indicated. The spectrum has been boxcar smoothed with a 2×2 window. Note the compact appearance of $H\beta$ at the spatial location of G1, compared with $[OIII]$, which suggests that at this location the line is excited mostly locally, rather than by the quasar (see text). The diagnostic diagram shows that the nuclear line ratios (blue solid circle) and those of the eastern EELR (cyan solid square) are successfully explained by AGN photoionization. G1 (open red circle) overlaps with the HII galaxy region, and this suggests that the gas is photoionized by young stars in this galaxy. Other symbols and lines as in Fig. 3.

preferentially emitted by the quasar associated EELR. On the contrary, $H\beta$ and $[OII]$ present a discontinuous, asymmetric spatial distribution, with a compact appearance at the G1 location (see Fig. 15). This suggests that these two low-ionization lines are emitted preferentially by G1, while $[OIII]$ has a relatively stronger contribution from the quasar EELR.

The linewidths add further information. $[OIII]$ has similar FWHM at the location of G1 (280 ± 30 km s $^{-1}$) and the western EELR (260 ± 30 km s $^{-1}$), while the low-ionization $[OII]$ line is, on the contrary, considerably narrower with FWHM = 200 ± 50 km s $^{-1}$ for G1. The intrinsic width is actually narrower, since we have not taken into account that $[OII]$ is a doublet. The values at the western EELR are 300 ± 20 and 450 ± 30 km s $^{-1}$ for $H\beta$ and $[OII]$, respectively. Unfortunately, the blue wing of $H\beta$ for G1 lies at the sharp edge of a deep atmospheric absorption band, so the FWHM = 140 km s $^{-1}$ is highly uncertain (this does not affect the western EELR because of its slightly higher z).

The results described above can be explained if $[OII]$ and $H\beta$ are emitted preferentially by G1, while $[OIII]$ has a relatively large contribution of flux from the quasar EELR. This implies that G1 is at the same z as the quasar. The nuclei of both objects are separated by ~ 3 arcsec or 20 kpc in projection. G1 is blueshifted in velocity by -110 ± 10 km s $^{-1}$ relative to the quasar.

We have extracted 1D spectra for G1 (see Fig. 17), the quasar and the western EELR. The apertures are shown in Fig. 16 (top). The location in the diagnostic diagram is shown in the same figure (bottom). The $H\beta$ flux of the quasar is affected by atmospheric absorption. We have corrected for this effect taking into account that $H\delta/H\gamma = 0.53 \pm 0.02$ is consistent with no reddening. The real $H\beta$ flux is estimated assuming $H\gamma/H\beta = 0.47$, the case B recombination

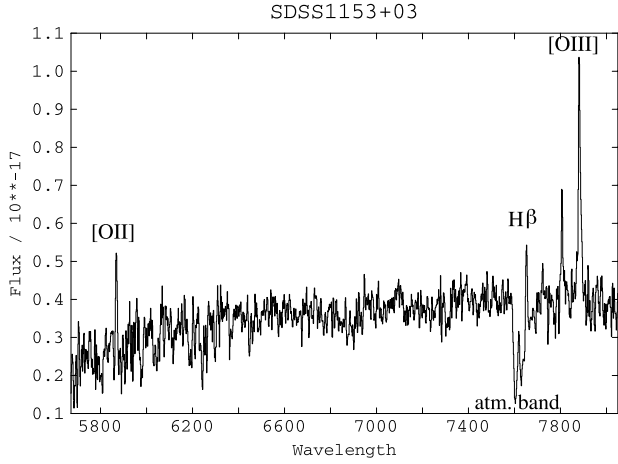


Figure 17. Spectrum of the companion galaxy G1 of SDSS J1153+03. $H\beta$ is absorbed by an atmospheric absorption band.

value. This gives $H\beta = (9.6 \pm 0.9) \times 10^{-16} \text{ erg s}^{-1} \text{ cm}^{-2}$, which is the value we have used in the diagnostic diagram. As expected, the quasar nuclear line ratios lie very far from the $H\text{II}$ galaxy region and are consistent with the AGN model sequence (it also emits He II ; Table 2).

The spectrum at the location of G1 overlaps with the region occupied by $H\text{II}$ galaxies. It could not be corrected for line reddening, since $H\gamma$ and $H\delta$ are not detected. As we mentioned above, line reddening could move an AGN to the $H\text{II}$ galaxy region in the $[\text{O III}]/H\beta$ versus $[\text{O II}]/H\beta$ diagram. However, the atmospheric absorption works in the opposite way. Looking at the spectrum, we estimate that at least 50 per cent of the $H\beta$ flux has been absorbed. Correcting for this $[\text{O III}]/H\beta$ would be ~ 1.5 , even lower than already observed and more typical of $H\text{II}$ galaxies than AGNs.

The spectrum of the quasar western EELR is consistent with AGN photoionization. Reddening would move it even further away from the $H\text{II}$ galaxies.

We propose that SDSS J1153+03 is interacting with a companion star-forming galaxy, where the gas is at least partially photoionized by young stars, which have probably been formed as a consequence of the interaction. The quasar is also associated with an ionized nebula which extends for 8 arcsec or $\sim 52 \text{ kpc}$ along PA 65.

3.8 SDSS J1228+00 ($z = 0.575$)

The narrow-band continuum image is shown in Fig. 18, and the 2D $H\beta$ -[O III] spectrum appears in Fig. 19. The spatial profile of the [O III] line is unresolved ($\text{FWHM} = 1.56 \pm 0.04 \text{ arcsec}$ versus $\text{FWHM} = 1.6 \pm 0.1 \text{ arcsec}$ seeing) along this direction. There is no evidence for extended line emission at $\text{SB} \gtrsim 3\sigma = 3 \times 10^{-18} \text{ erg s}^{-1} \text{ cm}^{-2} \text{ arcsec}^{-2}$ (Fig 19). G1 is a continuum source of unknown redshift.

The nuclear spectrum of this quasar (Fig. 1) is quite particular, since it shows very broad lines with $\text{FWHM} \gtrsim 1400 \text{ km s}^{-1}$.

This is a radio-intermediate quasar (see Section 2). It is known that the radio structures are capable of inducing strong kinematic perturbation in the gas, not only in radio loud (e.g. Villar-Martín et al. 1999), but also radio-quiet AGNs (e.g. Axon et al. 1998). However, a more plausible scenario is that we are looking close to the edge of the obscuring torus, so that we detect emission from an intermediate-density region ($10^4 < n < 10^6 \text{ cm}^{-3}$) between the BLR and NLR where the lines would also have intermediate FWHM. This is suggested by the difference in

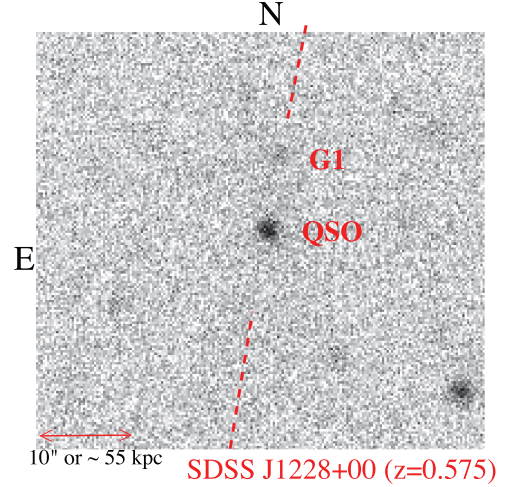


Figure 18. Narrow-band continuum image of the field around SDSS J1228+00. It was obtained with the $H\alpha+83$ FORS2 filter and covers the rest-frame spectral range $\sim 4150\text{--}4185 \text{ \AA}$. The PA 170 slit location is indicated. G1 is a continuum source of unknown z .

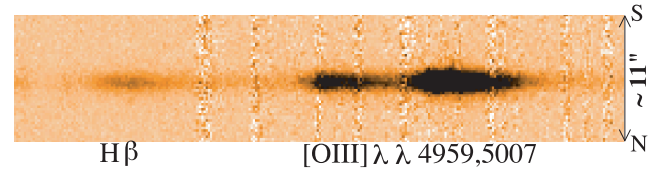


Figure 19. $H\beta$ -[O III] 2D spectrum of SDSS J1228+00. No extended line emission is detected.

width between forbidden lines with high and low critical densities (n_{crit}). We measure $\text{FWHM}([\text{O III}]) = 2000 \pm 200 \text{ km s}^{-1}$, $\text{FWHM}[\text{Ne III}] \sim 2200 \pm 200 \text{ km s}^{-1}$ and $\text{FWHM}[\text{O II}] = 1440 \pm 60 \text{ km s}^{-1}$. The critical densities of these lines are $n_{\text{crit}} \sim 10^6 \text{ cm}^{-3}$ for [O III], $\sim 10^7 \text{ cm}^{-3}$ for [Ne III] and $\sim 3 \times 10^3 \text{ cm}^{-3}$ for [O II]. Therefore, [O II] would be very efficiently quenched in the intermediate-density region, and it is more efficiently produced in lower density gas where the motions are also slower. The large $[\text{O III}]/H\beta$ ratio 12 ± 1 suggests that the intermediate-density region is very highly ionized. This could be part of the FHIL region discussed in Section 3.7.

3.9 SDSS J1307-02 ($z = 0.310$)

The morphology of this quasar in the broad-band image (Fig. 20) is asymmetric and elongated in the EW direction. Faint and diffuse emission is detected well beyond the optical size of the host galaxy with a measured total extension of $\sim 15 \text{ arcsec}$ or 82 kpc . Two long filaments reminiscent of tidal tails extend towards the east and north-east (NE). They appear as well in a narrow-band line-free image obtained with the $H\alpha/4500+61$ filter (not shown here) and emit mostly continuum. These features are evidence for mergers/interactions.

Fig. 21 (top) shows the $H\beta$ -[O III] 2D spectrum along PA 76. The [O III] spatial profile is dominated by a compact component with $\text{FWHM} = 1.06 \pm 0.02 \text{ arcsec}$. The stability of the seeing size during the spectroscopic observations ($\text{FWHM} \sim 0.83 \pm 0.03 \text{ arcsec}$ at the beginning versus $0.75 \pm 0.01 \text{ arcsec}$ at the end) implies that this central component is spatially resolved. In addition, low SB line emission is detected across a total extension of 10 arcsec or 55 kpc .

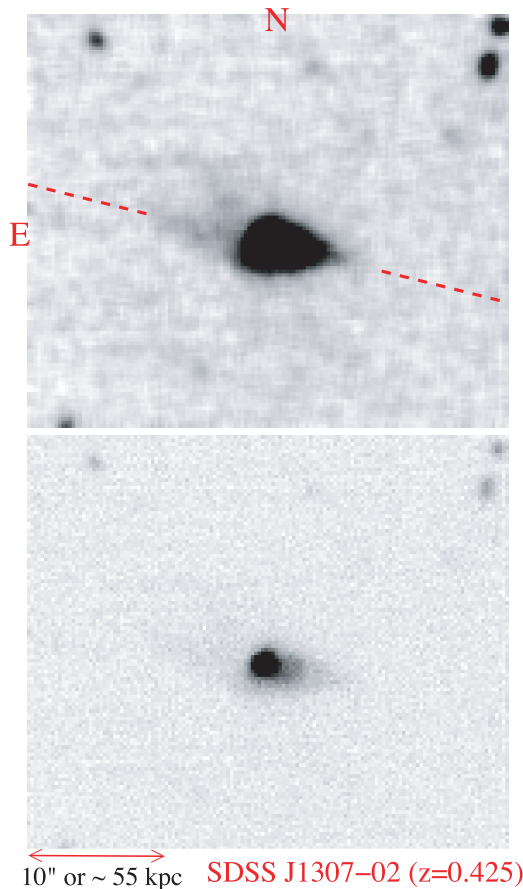


Figure 20. Broad-band image of the field around SDSS J1307–02. It was obtained with the V_High filter and covers the rest-frame spectral range 3462–4327 Å. The location of the PA 76 slit is indicated. The image on the top panel has been smoothed with a 3×3 window. Two filaments stretch towards the east and NE. They are reminiscent of tidal tails. The bottom image (non-smoothed) is shown with a different contrast to highlight features in the inner, brighter region.

The [O III] extension towards the west overlaps with a region of diffuse, faint continuum emission. Very faint continuum is also detected coinciding with the eastern filament mentioned above.

We have extracted 1D spectra from four apertures indicated in Fig. 21 (top). The faintest [O III] extended emission is detected in aperture 4 and has SB $5 \times 10^{-18} \text{ erg s}^{-1} \text{ cm}^{-2} \text{ arcsec}^{-2}$.

The line ratios are plotted in the diagnostic diagram in Fig. 21 (bottom). As expected, the quasar nuclear line ratios are better explained by AGN photoionization (the spectrum shows also strong He II; Table 3). The line ratios of Ap.1 (the adjacent eastern EELR) have large errors because H β is rather noisy, but they are very far from the H II galaxies and more consistent with AGN photoionization. Ap.3 and Ap.4 on the western EELR overlap with the H II galaxy region (only lower limits could be calculated for Ap.4). No useful limits on the line reddening could be estimated. This could be an example of an object where the EELR associated with the quasar is partially ionized by stars, although line reddening should be estimated before raising conclusions.

This region emits strong continuum, although the origin is uncertain. The [O III] FWHM values are 410 ± 30 , 420 ± 20 and $530 \pm 30 \text{ km s}^{-1}$ for Ap.1, Ap.2 and Ap.3, respectively (the Ap.4 spectrum is noisy). The lines are therefore relatively broad across the whole EELR extension.

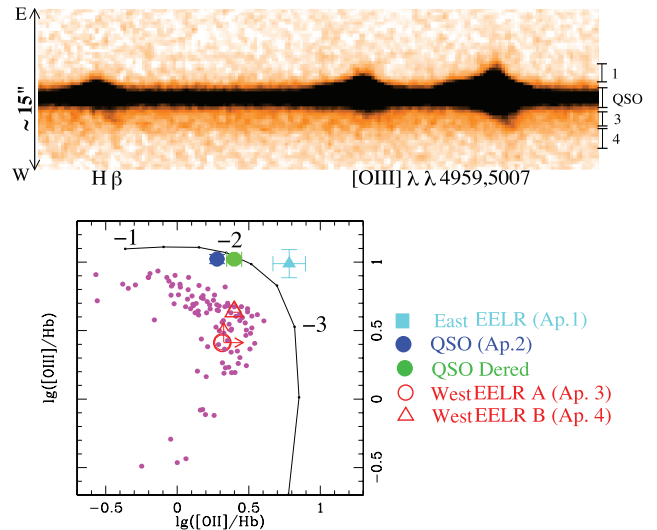


Figure 21. H β –[O III] 2D spectrum of SDSS J1307–02 along PA 76 (top). The original spectrum has been boxcar smoothed with a 2×2 window. The apertures used for the spectroscopic analysis are indicated on the right-hand side. The location of the quasar nuclear region (blue and green solid circles) and the eastern EELR (cyan solid square) are more consistent with AGN photoionization and lie very far from the H II galaxies. The western EELR (red open circle) overlaps with the H II galaxy region. Other symbols and lines as in Fig. 3.

Thus, SDSS J1307–02 shows morphological evidence for mergers/interactions. This quasar is associated with an ionized nebula which extends for ~ 10 arcsec or 55 kpc along PA 76. Although the nuclear gas and the eastern nebula are preferentially photoionized by the quasar, the possibility that the western nebula is photoionized by young stars is not discarded.

3.10 SDSS J1337–01 ($z = 0.329$)

The narrow band image is shown in Fig. 22. The [O III] spatial profile (Fig. 23) is dominated by an unresolved component (FWHM = 1.40 ± 0.04 arcsec versus 1.47 ± 0.09 seeing). In addition, very faint

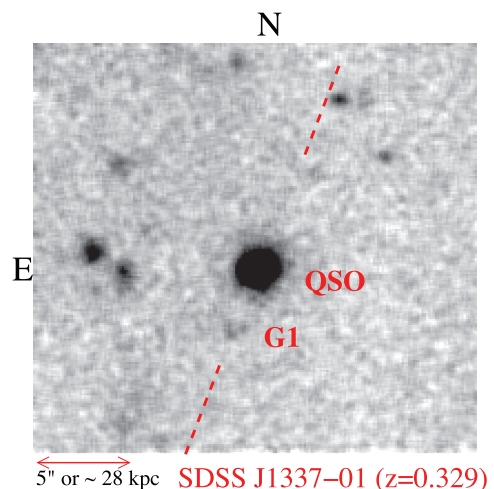


Figure 22. Narrow-band continuum image of SDSS J1337–01 obtained with the He II/6500+49 FORS2 filter. It covers the rest-frame spectral range ~ 3572 – 3623 Å. The location of the PA 159 slit is indicated. The original image has been boxcar smoothed with a 4×4 window. G1 is a continuum source of unknown z .

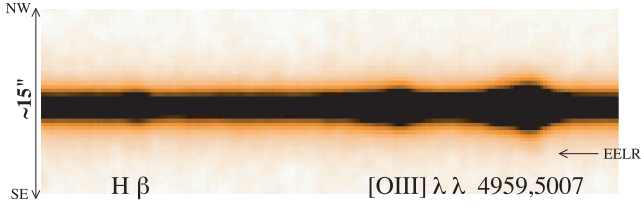


Figure 23. $H\beta$ -[O III] 2D spectrum of SDSS J1337-01 along PA 159. The original spectrum has been boxcar smoothed with a 4×4 window. Very faint extended [O III] emission is detected up to ~ 3.5 arcsec from the continuum centroid (indicated with ‘EELR’).

emission is detected towards the south-east along PA 159 extending up to 3.5 arcsec or ~ 20 kpc from the continuum centroid. The SB of this EELR is $\sim 10^{-17}$ erg s^{-1} cm^{-2} arcsec $^{-2}$. The [O III] spectral profile is unresolved and has FWHM $\lesssim 170$ km s^{-1} , compared with the much broader nuclear line (FWHM 930 ± 20 km s^{-1}). The EELR is shifted by just -25 ± 20 km s^{-1} relative to the nuclear [O III] emission. The spectrum is too noisy to perform any further kinematic and ionization analysis.

The nuclear line ratios are shown in Table 3. The $H\beta$ flux is heavily affected by underlying stellar absorption from the galaxy. The errors on the line ratios and the $H\beta$ flux do not account for this uncertainty.

The G1 spectrum shows that it is a continuum source of unknown z , maybe a star.

3.11 SDSS J1407+02 ($z = 0.309$)

The narrow-band continuum image is shown in Fig. 24. The [O III] spatial profile (Fig. 25) is dominated by a compact component of FWHM = 0.80 ± 0.3 arcsec (versus 0.73 ± 0.04 arcsec), which is consistent with being unresolved. There is no evidence for extended line emission at SB $\gtrsim 3\sigma = 3.2 \times 10^{-18}$ erg s^{-1} cm^{-2} arcsec $^{-2}$.

The G1 spectrum shows that it is a galaxy at $z = 0.254$ and therefore unrelated to the quasar.

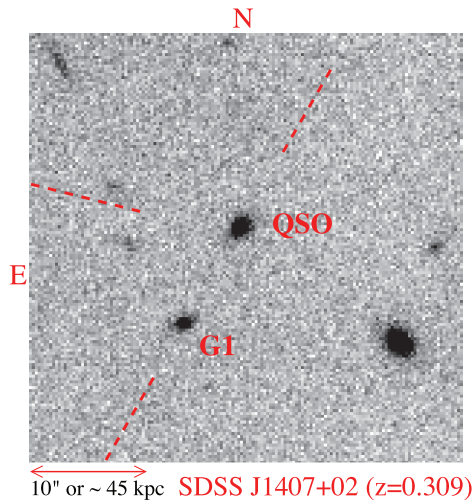


Figure 24. Narrow-band continuum image of SDSS J1407+02 obtained with the He II/6500+49 FORS2 filter. It covers the rest-frame spectral range 3625–3680 Å. The PA 150 slit is indicated. The original image has been boxcar smoothed with a 2×2 window. G1, which falls also within the slit, is galaxy at $z = 0.254$.

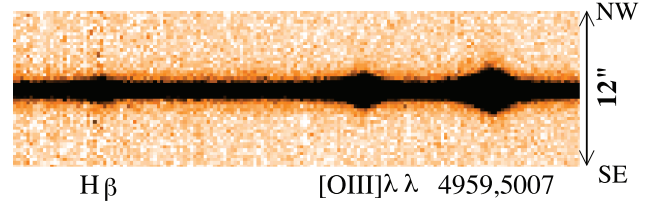


Figure 25. $H\beta$ -[O III] 2D spectrum of SDSS J1407+02. There is no evidence for extended line emission along PA 150.

3.12 SDSS J1413-01 ($z = 0.380$)

The broad band image is shown in Fig. 26. The [O III] spatial profile (Fig. 27) is dominated by a Gaussian component of FWHM 1.32 ± 0.04 arcsec, i.e. narrower than the seeing measured from stars in the images (1.54 ± 0.09 arcsec), indicating that the seeing improved during the spectroscopic exposure. There is no evidence for extended line emission along PA 45 for SDSS J1413-01 at SB $\gtrsim 3\sigma = 2 \times 10^{-18}$ erg s^{-1} cm^{-2} arcsec $^{-2}$.

3.13 SDSS J1546-00 ($z = 0.383$)

The broad band image is shown in Fig. 28. The [O III] spatial profile (Fig. 29) is dominated by a compact component of FWHM = 0.97 ± 0.02 arcsec (versus seeing FWHM = 0.90 ± 0.01). Taking errors into account and possible seeing smear during the spectroscopic exposure, this is compatible with this component being unresolved.

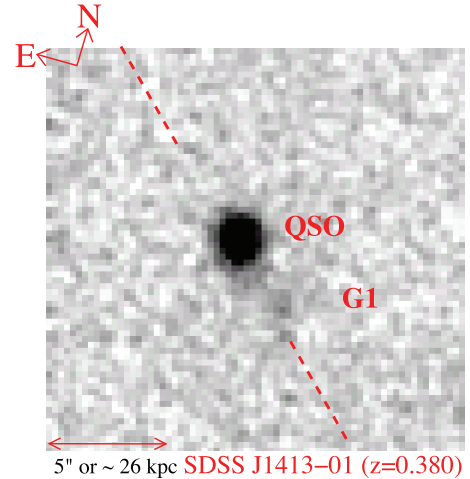


Figure 26. Broad-band image of SDSS J1413-01 obtained with the V_High filter which covers the rest-frame spectral range ~ 3575 – 4470 Å. The PA 45 slit is indicated. The original image has been boxcar smoothed with a 2×2 window. G1 is a faint source of unknown z .

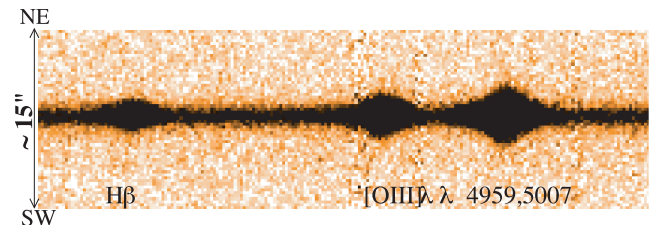


Figure 27. $H\beta$ -[O III] 2D spectrum of SDSS J1413-01. There is no evidence for extended line emission along PA 45.

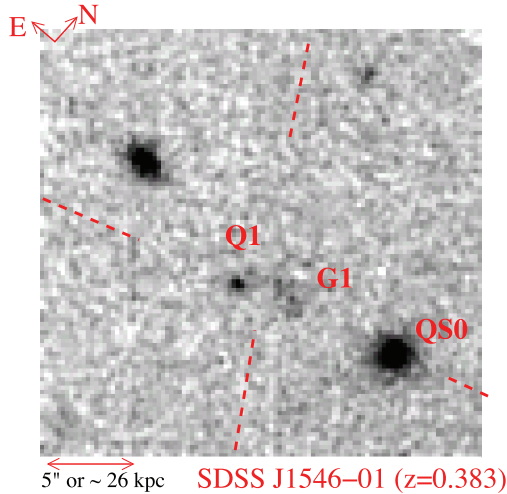


Figure 28. Broad-band V_{High} image of the field around SDSS J1546-00 (identified with QS0). It covers the rest-frame spectral range $\sim 3570\text{--}4460\text{ \AA}$. The PA 109 slit location is indicated. The original image has been boxcar smoothed with a 2×2 window. G1 and Q1 fall also within the slit.

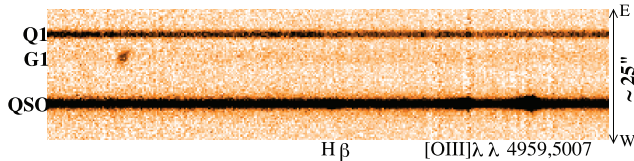


Figure 29. $H\beta$ -[O III] 2D spectrum of SDSS J1546-00. Note the emission line from G1, which places the object at most probably $z = 0.74$. Q1 is a type 1 quasar at $z = 4.12$.

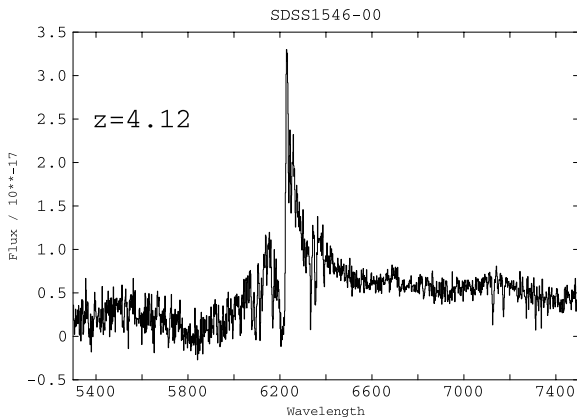


Figure 30. $\text{Ly}\alpha$ spectrum of the quasar Q1 along the slit of SDSS J1546-00 (Figs 28 and 29).

There is no evidence for extended line emission along PA 45 for SDSS J1546-00 at $\text{SB} \gtrsim 3\sigma = 3.8 \times 10^{-18} \text{ erg s}^{-1} \text{ cm}^{-2} \text{ arcsec}^{-2}$.

Q1 (Fig. 28) is a quasar at $z = 4.12$ (Fig. 30). G1 is an emission-line galaxy with a single detected line. It could be [O II] $\lambda 3727$ at $z = 0.747$ or $\text{Ly}\alpha$ at $z = 4.36$.

The nuclear line ratios are shown in Table 3. The strength of [O III] $\lambda 4363$ relative to [O III] $\lambda 5007$ suggests unusually high electron temperatures ($45000 \pm 10000 \text{ K}$). $T_e > 30000 \text{ K}$ is also implied by the SDSS spectrum.

4 DISCUSSION AND CONCLUSIONS

Table 4 is a summary of the results presented in Section 3. For each object it is specified whether an EELR has been detected and its nature. When an EIN, other than features such as tidal tails or bridges (see Section 3), has been detected, the maximum size measured along the slit is given in arcsec and kpc. We emphasize that in most cases there is no information available about the possible existence of extended line emission along other directions.

In column 6, we specify whether other emission-line features have been found, such as star-forming companion galaxies, knots and/or nuclei. In column 7, we say whether there is evidence for galaxy mergers/interactions. The VLT-FORS2 nuclear [O III] luminosity and the SDSS [O III] luminosity are shown in columns 9 and 10. We have added the information on SDSS J0123+00 ($z = 0.399$), observed as part of the same observational programme (Villar-Martín et al. 2010).

The summary of our results is presented next. As we mentioned in Section 3, they cannot be generalized to all optically selected type 2 quasars, due to different possible biases.

(i) Evidence for galaxy mergers/interactions is found in 6/14 objects (SDSS J2358-00, SDSS J0217-00, SDSS J0025-10, SDSS 1153+03, SDSS J1307-02, SDSS J0123+00). Such evidence was suggested by other authors for SDSS J2358-00 and SDSS J0123+00 (Zakamska et al. 2006) based on *HST* images.

The detection rate in our sample is possibly higher. Our images are rather shallow for most objects, and the rate of detection of the characteristic morphological features indicative of mergers/interactions depends on the depth of the images. For comparison, this rate is very high in powerful radio galaxies (75–95 per cent; Ramos Almeida et al. 2011).

(ii) Evidence for recent star formation in the neighbourhood of the quasars is found for 5/14 objects. The star formation is happening in general in companion galaxies (SDSS J2358-00, SDSS 1153+03, SDSS J0123+00), knots (SDSS J0217-00, SDSS J0025-10) and/or a nuclei (SDSS J0025-10). Star formation is possibly happening as well in the tidal bridge that connects SDSS J0123+00 with its interacting companion (Villar-Martín et al. 2010). All these objects show evidence for mergers/interactions, which could be responsible for triggering the star formation activity.

As mentioned earlier, AGN photoionization cannot be completely discarded in favour of stellar photoionization based only on the ratios studied here. Other properties such as the narrowness of the emission lines and the spatial morphology favour the stellar photoionization scenario. This is further supported by the fact that those regions with line ratios consistent with H II galaxies are in general companion galaxies, nuclei, knots and tidal features associated with quasars which are undergoing a merger event, where active star formation is naturally expected. In addition, if the gas was photoionized by the AGN, this would mean that in all cases the companion knots/nuclei/galaxy/tidal tails are within the quasar ionization cones, which is quite unlikely.

SDSS J1307-02 also shows morphological evidence for mergers/interactions. This might be another object with star formation, although it is necessary to determine the impact of line reddening before raising a definitive conclusion.

Therefore, we find a diverse population of systems. Several (particularly those with high SB off-nuclear structures indicative of mergers) are composite in their emission-line properties showing a combination of AGN and star formation features. It is possible that at least some of the radio-quiet type 2 quasars are triggered in galaxy

Table 4. Summary of results. For each object it is specified whether an EELR has been detected or not (column 2) and its nature: extended ionized nebula (EIN); tidal tail (TT) and tidal bridge (TB). When an EIN is detected, the maximum measured size is given in arcsec and kpc (columns 4 and 5). Column 6 indicates whether other emission-line features have been found and their nature: star-forming companion galaxy (SFCG), star-forming companion nucleus (SFCN), star-forming knot (SFCK). In Columns 7 and 8, it is said whether the object shows signs of mergers/interactions (7) and star formation (8). The nuclear [O III] luminosity measured from the VLT-FORS2 spectra is given in column 9 relative to the solar luminosity and in log. The [O III] luminosity measured from the SDSS spectra (3-arcsec fibres) is given in column 10 (taken from Zakamska et al. 2003). The objects observed in the 2008 and 2009 runs are separated (upper and lower parts, respectively).

Object	EELR	Nature	Max. size of EIN (arcsec)	Max. size of EIN (kpc)	Other features?	Interactions?	SF?	L([O III]) _{nuc}	L([O III]) _{SDSS}
(1)	(2)	(3)	(4)	(5)	(6)	(7)	(8)	(9)	(10)
SDSS J2358–00	Yes	EIN	12	64	SFCG	Yes	Yes	9.27	9.32
SDSS J0025–10	Yes	TT	–	–	SFCN, SFCK	Yes	Yes	8.60	8.73
SDSS J0217–00	Yes	EIN	4	19	SFCN	Yes	Yes	8.81	8.75
SDSS J0234–00	No	–	–	–	No	No	No	8.73	8.77
SDSS J0849+01	No	–	–	–	No	No	No	8.14	8.06
SDSS J0955+03	Yes	EIN	7.5	38.5	No	No	No	8.04	8.60
SDSS J1153+03	Yes	EIN	8	52	SFCG	Yes	Yes	9.54	9.61
SDSS J1228+00	No	–	–	–	No	No	No	9.06	9.28
SDSS J1307–02	Yes	EIN	10	55	No	Yes	?	8.91	8.92
SDSS J1337–01	Yes	EIN	3.5	20	No	No	No	8.50	8.72
SDSS J1407+02	No	–	–	–	No	No	No	9.23	8.90
SDSS J1413–01	No	–	–	–	No	No	No	8.97	9.25
SDSS J1546–00	No	–	–	–	No	No	No	8.24	8.18
SDSS J0123+00 ^a	Yes	TB, EIN	34	180	SFCG?	Yes	Yes	9.02	9.13

^aSee Villar-Martín et al. (2010) for results on SDSS J0123+00.

major interactions involving at least one gas-rich galaxy, although it is essential to compare the rate of detection of mergers/interactions with that of a non-active galaxy control sample.

Since at least some of the star-forming regions of the type 2 quasars would be included in the SDSS aperture, this might explain the type 2 quasars with composite AGN/star formation spectra (Villar-Martín et al. 2008).

This result seems different from that obtained for powerful radio galaxies in which, based on the analysis of the extended line emission, there seems to be less such evidence. Although 20–30 per cent of radio galaxies show evidence for star formation from their continuum properties, in many of these cases the young stellar populations are relatively old and do not produce significant emission lines (Tadhunter et al. 2005; Tadhunter 2011). The radio galaxy PKS 1932–464 at $z = 0.23$ (Villar-Martín et al. 2005) is a remarkable exception.

We do not know whether star formation is ongoing or has recently happened *within* the host galaxies of the quasars studied here, except for SDSS J1337–01, where Bian (2007) found a very young stellar population. Intense star formation activity would not be surprising, since different works suggest that radio-quiet type 2 quasars at similar z have very high star-forming luminosities, much higher than field galaxies (e.g. Lacy et al. 2007; Zakamska et al. 2008; Hiner et al. 2009).

(iii) 8/14 objects have EELRs. In most cases (7/8) the EELR apparently consists of an EIN associated with the quasar. For one object (SDSS J0123+00), moreover, a tidal bridge is also a part of the EELR. For another quasar, the EELR consists of a tidal tail (SDSS J0025–10). The detection rate of EELRs in our sample is a lower limit, since the results presented here refer in most cases to a single blind spatial direction.

The sizes of the EINe vary between several kpc and up to 64 kpc (180 kpc, including SDSS 0123+00). At the detection limit of our data, the non-detection of EELRs implies that, if existing, the size along the studied direction is \leq few kpc. Greene et al. (2011) find that ionized gas is ubiquitous within the quasar host galaxies but rare at larger spatial scales ($\gtrsim 10$ kpc). However, these authors reach much shallower SB levels $\sim 10^{-16}$ erg s^{−1} cm^{−2} arcsec^{−2}.

Humphrey et al. (2010) found EELRs associated with two out of six type 2 SDSS quasars with maximum total sizes of ~ 40 and 27 kpc, respectively. We emphasize that these data were $\gtrsim 10$ times shallower than those presented here.

As we explained in Section 1, studies of type 1 quasars show that luminous ($L[\text{O III}] > 5 \times 10^{41}$ erg s^{−1}) EELRs are preferentially associated with steep spectrum radio-loud quasars with high nuclear line luminosities ($L[\text{O III}]_{\text{nuc}} > 6.5 \times 10^{42}$ erg s^{−1}; Fu & Stockton 2007, 2009). Our data are too limited to make a proper comparison, since we would require a complete spatial coverage around the type 2 quasars and an accurate measurement of the total EELR [O III] luminosity. However, there are two objects which are worth mentioning: SDSS J0123+00 and SDSS J2358–00. The [O III] EELR luminosities measured from the spectra (therefore, these are lower limits) are $(3.05 \pm 0.08) \times 10^{42}$ erg s^{−1} and $(5.1 \pm 0.1) \times 10^{41}$ erg s^{−1}, respectively. Neither object is radio loud, therefore these two examples demonstrate that a luminous EELR is not necessarily associated with a powerful radio source.

The nuclear [O III] luminosities are 7.2×10^{42} and 4.4×10^{42} erg s^{−1} for SDSS2358–00 and SDSS J0123+00, respectively (we have tried to use an aperture similar in physical size to that used by Fu & Stockton 2009). Both are close to the minimum nuclear

$L[\text{O III}]$ found by these authors for quasars with luminous EELRs.²

(iv) We have investigated the gas ionization mechanism in the EELRs of five quasars where this study was possible. Stellar photoionization is very probably present in the tidal tail and tidal bridge of SDSS J0025–10 (this work) and SDSS J0123+00 (Villar-Martín et al. 2010), respectively; maybe also in the EELR of SDSS J1307–02. The EINE are preferentially photoionized by the quasar in at least four of them (SDSS J2358–00, SDSS 1153+03, SDSS J1307–02 and SDSS J0123+00).

(v) The nuclear gas is preferentially photoionized by the active nucleus. The $H\beta$ luminosities measured for the quasars in our sample are in the range $L_{H\beta} \sim (0.2\text{--}9.3) \times 10^{41} \text{ erg s}^{-1}$. Similar values have been measured for the NLR of some radio-quiet type 1 quasars (e.g. Bennert et al. 2002). The implied photon ionizing luminosity $Q_{\text{ion absorbed}}$ by the gas is given by $Q_{\text{ion}} = \frac{L_{H\beta}}{h\nu_{H\beta}} \times \frac{\alpha_B}{\alpha_{H\beta}^{\text{eff}}}$, where $h\nu_{H\beta}$ is the energy of a $H\beta$ photon and α_B and $\alpha_{H\beta}^{\text{eff}}$ are the total and effective $H\beta$ case B hydrogen recombination coefficients (Osterbrock 1989). Q_{ion} is in the range $\sim (0.08\text{--}4) \times 10^{54} \text{ s}^{-1}$.

In the previous section, we derived $\log(U)$ for four objects from the AGN models, which is in the range from -1.3 to -2.0 . Using the corresponding $L(H\beta)$ values and $U = \frac{Q}{4\pi r^2 n c}$ (Section 3), a $n = 100 \text{ cm}^{-3}$ density implies $r \sim 500 \text{ pc}$ to 1.5 kpc . NLR sizes of type 1 quasars measured from *HST* images are ~ 1 to several kpc (Bennert et al. 2002). It should be kept in mind that the r values we have inferred refer to the region that emits the bulk of the line emission, while the actual radius of the NLR could be larger.

(vi) Forbidden high ionization [Fe VII] lines have been detected in the nuclear spectrum of one object (SDSS J1153+03). Very broad underlying $H\beta$ and strong continuum are also detected. Based on previous works by other authors, we propose that this object is seen with a viewing angle intermediate between pure type 1 and type 2 orientations so that the illuminated face of the torus and regions interior to it can be at least partially observed. Emission from the intermediate region between the NLR and the BLR is possibly detected from SDSS J1228+00 as well. These are the highest z objects in our sample ($z = 0.575$).

ACKNOWLEDGMENTS

This work has been funded with support from the Spanish Ministerio de Ciencia e Innovación through the grants AYA2004-02703, AYA2007-64712 and AYA2009-13036-C02-01 and co-financed with FEDER funds. We thank the referee for the thorough revision of the original manuscript and very useful comments that helped to improve the paper. Thanks to the staff at Paranal Observatory for their support during the observations.

REFERENCES

Antonucci R., 1993, *ARA&A*, 31, 473
Appenzeller I. et al., 1998, *The Messenger*, 94, 1

² The comparison of the [O III] nuclear luminosities should be considered with caution, since [O III] has high critical densities and it can be partially produced in regions which are not observable for type 2 quasars. That is, the [O III] line luminosity depends on orientation (e.g. di Serego Alighieri et al. 1997). According to this, for a type 1 orientation (as Fu and Stockton objects), we would measure a higher nuclear [O III] luminosity.

- Axon D., Marconi A., Capetti A., Maccetto F., Schreier E., Robinson A., 1998, *ApJ*, 496, L75
Bennert N., Falcke H., Schulz H., Wilson A., Wills B., 2002, *ApJ*, 547, 105
Bian W. H., 2007, in Ho L. C., Wang J. M., eds, *ASP Conf. Ser. Vol. 373, The Central Engine of Active Galactic Nuclei*. Astron. Soc. Pac., San Francisco, p. 675
Cisternas M. et al., 2011, *ApJ*, 726, 57
di Serego Alighieri S., Cimatti A., Fosbury R. A. E., Hes R., 1997, *A&A*, 328, 510
Fu H., Stockton A., 2007, *ApJ*, 664, L75
Fu H., Stockton A., 2008, *ApJ*, 677, 79
Fu H., Stockton A., 2009, *ApJ*, 690, 953
Greene J., Zakamska N., Ho L., Barth A., 2011, *ApJ*, 732, 9
Hiner K., Canalizo G., Lacy M., Sajina A., Armus L., Ridgway S., Storrie-Lombardi L., 2009, *ApJ*, 706, 508
Humphrey A., Villar-Martín M., Fosbury R., Vernet J., di Serego Alighieri S., 2006, *MNRAS*, 369, 1103
Humphrey A., Villar-Martín M., Sánchez S., Martínez-Sansigre A., González Delgado R., Pérez E., Tadhunter C., Pérez-Torres M., 2010, *MNRAS*, 408, L1
Jiang L., Fan X., Ivezić Z., Richards G., Scheneider D., Strauss M., Kelly B., 2007, *ApJ*, 656, 680
Lacy M., Sajina A., Petric A., Seymour N., Canalizo G., Ridgway E., Armus L., Storrie-Lombardi L., 2007, *ApJ*, 669, L61
Lal D. V., Ho L., 2010, *AJ*, 139, 1089
Lamareille F., Mouchine M., Contini T., Lewis I., Maddox S., 2004, *MNRAS*, 350, 396
Martínez-Sansigre A., Rawlings S., Lacy M., Fadda D., Marleau F., Simpson C., Willott C., Jarvis M., 2005, *Nat*, 436, 666
Miller L., Peacock J. A., Mead A. R., 1990, *MNRAS*, 244, 207
Mullaney J., Ward M., Done C., Ferland G., Schurch N., 2009, *MNRAS*, 394, L16
Nesvadba N., Lehnert M., Eisenhauer F., Gilbert A., Tecza M., Abuter R., 2006, *ApJ*, 650, 693
Osterbrock D. E., 1989, *Astrophysics of Gaseous Nebulae and Active Galactic Nuclei*. University Science Books, Mill Valley, CA
Penston M., Fosbury R., Boksenberg A., Ward M., Wilson A., 1984, *MNRAS*, 208, 347
Ptak A., Zakamska N., Strauss M., Krolik J., Heckman T., Schneider D., Birnkmann J., 2006, *ApJ*, 637, 147
Ramos Almeida C., Tadhunter C., Inskip K., Morganti R., Holt J., Dicken D., 2011, *MNRAS*, 410, 1550
Robinson A., Binette L., Fosbury R., Tadhunter C. N., 1987, *MNRAS*, 227, 97
Tadhunter C., Robinson T., González Delgado R., Wills K., Morganti R., 2005, *MNRAS*, 356, 480
Tadhunter C. N. et al., 2011, *MNRAS*, 412, 960
Terlevich R., Melnick J., Masegosa J., Moles M., Copetti M., 1991, *A&AS*, 91, 285
Villar-Martín M., Tadhunter C., Morganti R., Axon D., Koekemoer A., 1999, *MNRAS*, 307, 24
Villar-Martín M., Tadhunter C., Morganti R., Holt J., 2005, *MNRAS*, 359, L5
Villar-Martín M., Humphrey A., Martínez-Sansigre A., Pérez-Torres M., Binette L., Zhang X. G., 2008, *MNRAS*, 390, 218
Villar-Martín M., Tadhunter C., Humphrey A., Pérez E., Martínez-Sansigre A., González-Delgado R., Pérez-Torres M., 2010, *MNRAS*, 407, L6
York D. et al., 2000, *AJ*, 120, 1579
Zakamska N. et al., 2003, *AJ*, 126, 2125
Zakamska N., Strauss M., Heckman T., Ivezić Z., Krolik J., 2004, *AJ*, 128, 1002
Zakamska N. et al., 2005, *AJ*, 129, 1212
Zakamska N. et al., 2006, *AJ*, 132, 1496
Zakamska N., Gómez L., Strauss M., Krolik J., 2008, *ApJ*, 136, 1607

This paper has been typeset from a \LaTeX file prepared by the author.